POLITECNICO
MILANO 1863

SCUOLA DI INGEGNERIA INDUSTRIALE
E DELL'INFORMAZIONE

LES Simulation of Calcium Hydroxide discharge for Ocean Liming with coal carriers

Tesi di Laurea Magistrale in
Aeronautical Engineering - Ingegneria Aeronautica

Author: **Diego Bindoni**

Student ID: 964136
Advisor: Prof. Antonella Abbà
Academic Year: 2022-2023

Abstract

On both broad and local sizes, the consequences of pollution from human activities on the environment are observable and quantifiable, including glaciers melting, microplastics in food and air pollution in big cities. The acidity of the seas as a result of higher amounts of CO_2 in the atmosphere is a phenomenon that is less well-known to the general population. In reality, the sea absorbs a sizable amount of the available CO_2, which breaks down into bicarbonate, carbonate, and H^+ ions, raising the pH. Several marine species at the base of the food chain, like plankton, mollusks, and corals, are seriously threatened by the decrease in pH because it prevents the synthesis of calcium carbonate. The scientific community has examined the issue, and a number of technologies and strategies are still being researched and developed to help stop the acidification of the oceans. The so-called *Ocean Liming*, which entails releasing alkaline materials into the ocean to raise the pH and the capacity of CO_2 absorption, is one of the potential approaches on which the current thesis is founded.

The near wake portion of a common container ship is numerically simulated in the present work, in order to analyze the distribution of an alkaline material, in this case calcium hydroxide $CaOH_2$, and its effects on local marine pH. Simulations were carried out for three cases of initial concentration, 2, 20 and 86.5 g/l, to observe a broad spectrum of how the solution can be used. LES simulations were performed using the unsteady and reactive solver *reactingFoam*, implemented in the opensource software *OpenFOAM*. Computational resources were provided by the CINECA computing centre, which provided the computing hours for this project on the Galileo 100 super-computer. Propeller motion was modelled using a Multi Reference Frame approach, allowing a more accurate representation of the fluid-dynamics of the problem in the near-wake zone.

Simulations were performed for each case, in a non-reactive and a reactive version, in order to quantify the effect of the chemistry. Once the results were obtained, preliminary analyses were made on the vortex structures formed, and then on the distribution of $CaOH_2$, OH^- and pH accordingly.

Keywords: Ocean Liming, Calcium hydroxide, LES simulations, OpenFOAM

Sommario

Le conseguenze dell'inquinamento delle attività umane sull'ambiente sono osservabili e quantificabili sia a livello locale che globale, come lo scioglimento dei ghiacciai, la presenza di microplastiche negli alimenti e l'inquinamento atmosferico nelle grandi città. L'acidità dei mari, conseguenza dell'aumento della quantità di CO_2 nell'atmosfera, è un fenomeno meno noto. L'oceano infatti assorbe una notevole quantità di CO_2 dall'atmosfera, che si scompone in acqua generando ioni bicarbonato, carbonato e H^+, diminuendo il pH. Diverse specie marine alla base della catena alimentare, come il plancton, i molluschi e i coralli, sono seriamente minacciate dalla diminuzione dei livelli di pH poichè impedisce la sintesi del carbonato di calcio. La comunità scientifica ha esaminato il problema e sono ancora in fase di ricerca e sviluppo numerose tecnologie e strategie per contribuire a fermare l'acidificazione degli oceani. Il cosiddetto *Ocean Liming*, che prevede il rilascio di materiali alcalini nell'oceano per aumentare il pH e la capacità di assorbimento di CO_2, è uno dei potenziali approcci su cui si basa questa tesi.
Il progetto in questione simula la porzione di scia prossima ad una comune nave da trasporto, al fine di analizzare la distribuzione di un materiale alcalino, in questo caso idrossido di calcio $CaOH_2$, e i suoi effetti sul pH marino locale. Le simulazioni sono state effettuate per tre casi di concentrazione iniziale, ovvero 2, 20 e 86,5 g/l, per osservare un ampio spettro di utilizzo della soluzione. Le simulazioni LES sono state eseguite utilizzando il solver instazionario e reattivo *reactingFoam*, implementato nel software open-source *OpenFOAM*. Le risorse di calcolo sono state fornite dal centro di calcolo CINECA, che ha messo a disposizione le ore di calcolo utilizzate per questo progetto sul supercomputer Galileo 100. Il moto dell'elica è stato modellato utilizzando un approccio Multi Reference Frame, che consente una rappresentazione più accurata della fluidodinamica del problema.
Le simulazioni sono state eseguite, per ogni caso, in versione non reattiva e reattiva, al fine di quantificare l'effetto della chimica. Una volta ottenuti i risultati, sono state effettuate analisi preliminari sulle strutture vorticose formate, seguite poi da una trattazione accurata della distribuzione di $CaOH_2$, OH^- e, di conseguenza, del pH.

Parole chiave: Ocean Liming, Idrossido di calcio, Simulazioni LES, OpenFOAM

Contents

Introduction

Pollution from human activities has effects on the surrounding environment that are visible and measurable on large and small scales, from melting glaciers, to microplastics in food, to air pollution in large cities. A phenomenon less known to the public community is the acidification of the seas, due to increased levels of CO_2 in the atmosphere. A significant portion of the CO_2 present in the atmosphere is in fact absorbed by the sea, which dissociates into bicarbonate, carbonate and H^+ ions, thereby lowering the pH. The decrease in pH poses a serious threat to the survival of many marine species at the base of the food chain, such as plankton, mollusks and corals, as it inhibits the production of calcium carbonate. The problem has been analyzed by the scientific community, and various technologies and approaches are still being studied and developed to counteract the acidification of the seas. One of the possible methods, on which the present thesis is based, is the so-called *Ocean Liming*, which consists of discharging alkaline substances into the ocean to increase the pH and the absorption capacity of CO_2.

Within the framework of the OL method, several tests of possible alkaline substances and injection methods have been made. In the present work, the method used follows the work done by S.Caserini [4], which involves the diffusion of calcium hydroxide $CaOH_2$ into the ocean through carbon carriers. LES simulations were performed using the open source program OpenFOAM, to develop a three-dimensional, reactive model of the wake generated by the ship's hull and propeller. A KRISO container ship with the injector placed behind the KP505 propeller was considered, as suggested by the results obtained by F.Argentieri [9]. The method used to simulate the blade motion is the Multiple Reference Frame. Using the solver *reactingFoam*, an accurate analysis of the near wake has been performed, analyzing the dissociation of calcium hydroxide and comparing pH values generated in different cases.
Here below a brief outline of the thesis will be presented:

- **Chapter 1**: presentation of the problem of $CaOH_2$, with a brief review of Ocean Liming method;

- **Chapter 2**: physical and fluid dynamic model;
- **Chapter 3**: numerical aspects of the problem;
- **Chapter 4**: mesh generation, boundary conditions and initial conditions of simulations. An analysis of mesh convergence and fluid-dyamic results;
- **Chapter 5**: reactive simulation's results, with a validation of the chemistry model adopted;
- **Chapter 6**: conclusions and future developments.

1 | The Ocean Liming

1.1. Ocean Acidification

As set out in one of the latest reports by the IPCC [3], anthropogenic pollution leads to deoxygenation, acidification and warming of the ocean, with catastrophic consequences for marine fauna and flora, including a decrease in species size, corrosion of shellfish shells and coral bleaching.

1.1.1. Carbon cycle and decrease of pH

Human activities pose a serious problem to the environment, threatening ecosystems through over-exploitation and emission of pollutants. In the specific case of the oceans, one of the greatest damages caused by humans is the emission of CO_2. Because of its high alkalinity and its large volume on Earth's surface, seawater is the largest inorganic C reservoir of Earth. Still, according to IPCC report on acidification of oceans [18], since the beginning of the industrial era, oceanic uptake of CO_2 has resulted in a worryng acidification of the ocean; the pH of ocean surface water has decreased by 0.1, corresponding to a 26 % increase in acidity, measured as hydrogen ion concentration.

The chemical phenomenon behind ocean acidification is the dissolution of carbon dioxide in water, presented in equation (1.1), due to a partial pressure difference of CO_2 between water and atmosphere (Renforth and Henderson [22]).

$$CO_{2(aq)} + H_2O \leftrightarrow H_2CO_3 \tag{1.1}$$

It has to be noted that CO_2 has been referred as aqueous since carbon dioxide is more concentrated in water than H_2CO_3. Once formed, the carbonic acid (H_2CO_3) quickly dissociates into a bicarbonate ion (HCO_3^-), which can in turn generate a carbonate ion

(CO_3^{2-}). In both reactions, an hydrogen ion is released, as can be seen from the equations:

$$H_2CO_3 \leftrightarrow HCO_3^- + H^+ \tag{1.2}$$

$$HCO_3^- \leftrightarrow CO_3^{2-} + H^+ \tag{1.3}$$

According to the formulae (1.2) and (1.3), an ion H^+ is then produced for each reaction, leading to a lowering of pH and a consequent acidification of the solution. The formula for calculating pH is:

$$pH = -\log_{10}[H^+] \tag{1.4}$$

where $[H^+]$ represents the concentration of hydrogen ions. In Figure 1.1, it can be seen how, due to difference in seawater composition and temperature, the the phenomenon is unevenly distributed across the oceans, with a more pronounced effect in areas closer to the earth's poles.

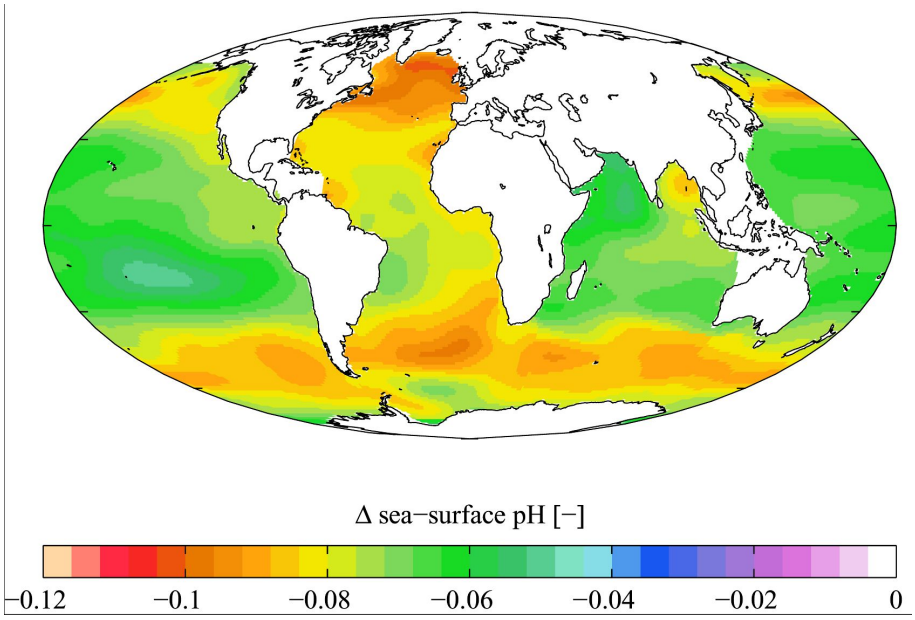

Figure 1.1: Estimated change in sea surface pH from preindustrial period (1700s) to the present day. Image retrieved from the Global Ocean Data Analysis Project [11].

1.1.2. Consequences of human pollution

We can identify several phenomena closely related to or entirely caused by the acidification of the seas.

In the first case, the pH degrowth is more pronounced at the poles, as the absorption

capacity of CO_2 increases if the water temperature decreases. This results in greater carbon dioxide uptake at the poles, as presented in an article by Union of Concerned Scientists [25], and consequently greater acidification of the waters present in those areas. As a related effect, warmer regions are also increasingly becoming sources of CO_2 rather than sinks.

In the second case, the imbalance in pH levels poses a serious threat to the survival of many marine species, particularly corals and molluscs, which process and produce calcium carbonate ($CaCO_3$, also called *calcite* or *aragonite*) for their shells and skeletons. Ocean's alkalinity [1] strongly depends on the concentration $CaCO_3$, trough its dissolution in carbonate (CO_3^{2-}) and calcium (Ca^{2+}) ions or its deposition in sea sediments (Doney [8].

$$CaCO_3 \leftrightarrow Ca^{2+} + CO_3^{2-} \tag{1.5}$$

Calcite's dissolution or formation rates are mainly governed by the concentration of calcium and carbonate ions through the staturation state (Ω), defined as:

$$\Omega = [Ca^{2+}][CO_3^{2-}]/K'_{sp} \tag{1.6}$$

where K'_{sp} is the apparent solubility product, which is a function of temperature, salinity, pressure. Since the concentration of calcium is proportional to salinity, the saturation state is largely determined by variations in carbonate ions. Thus, imbalances in alkalinity fluxes can affect the ocean's ability to store C, which is thought to play an important role in climate control. For this reason, knowledge of these natural processes has led to the development of artificial methods to control ocean chemistry.

1.2. Ocean liming

There are various strategies developed for preventing global climate changes, in particular global warming. In 1995 Kheshgi [12] was the first to come up with the idea of sequestering anthropogenic carbon dioxide adding alkalinity to seawater. Such approach is called "Ocean Liming" or "Ocean Alkalinization" and allows not only to prevent global warming, but also to counteract ocean acidification and strengthen reef calcification. The process consists in discharging $Ca(OH)_2$ (Portlandite, slaked lime or hydrated lime) in seawater, which dissociates in water as:

$$Ca(OH)_2 \leftrightarrow Ca^{2+} + 2(OH^-) \tag{1.7}$$

[1] Alkalinity is the capacity of a solution to neutralize acid.

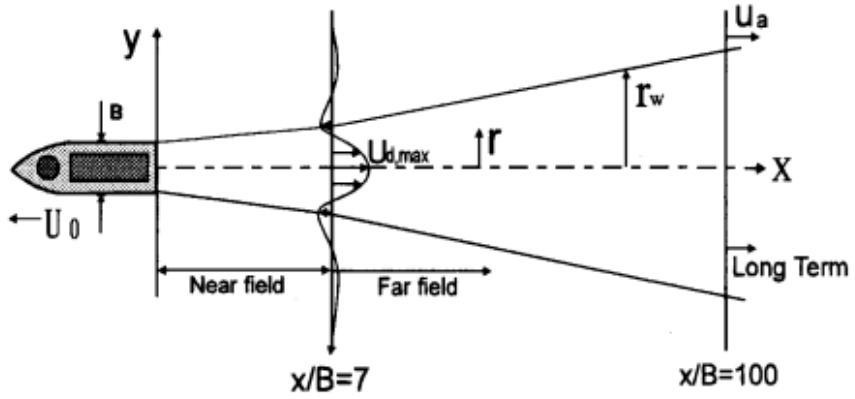

Figure 1.2: Schematic presentation of the three regimes in the wake of a ship, by [6]. U_0 represents

$$CO_2 + OH^- \leftrightarrow HCO_3^- \tag{1.8}$$

The ions can react with carbon dioxide forming HCO_3^-, as in equation (1.8), which further breaks up into CO_3^{2-} ions (equation (1.3), fundamental elements for the Ocean Alkalinity cycle. Morevore, Ca^{2+} can react with carbonate ions forming aragonite, or with bicarbonate generating $CaCO_3$ and carbon dioxide, as expressed resepctively in equations (1.5) and (1.9).

$$Ca^{2+} + 2HCO_3^- \leftrightarrow CaCO_3 + H_2O + CO_2 \tag{1.9}$$

In order to contain costs and emissions related to the supply chain of the activity, a promising strategy consists in the use of cargo ships to release carbon hydroxide in areas particularly prone to marine acidification (Caserini [4]): as visible from 1.1, Ocean Liming should be focused in the regions where the change in sea surface pH is more prominent, like in the north atlantic ocean, where the lowering of pH values reach absolute values up to 0.1.

1.2.1. Fluid dynamics of slurry in a ship's wake

Regarding the use of cargo ships's wake to better diffuse the slaked lime, a study from Chow [6] identifies three distinct zones inside the wake, as can ben seen in Figure 1.2.

In the *long term region* ($x/B > 100$), where B is the hull width, the slurry's diffusion depends only on marine currents and ambient turbulence. In the *far wake region*($7 <$

$x/B < 100$) is instead possible to formulate similarity profiles for the axial velocity (1.10).

$$U(x, r) = U_0 + U_{d,max}(x) f(r/r_w) \tag{1.10}$$

where r represents the radial distance from the centre of the propeller, U_0 represents the ship's cruising speed, U_d the velocity defect in center line, r_w the wake amplitude at a certain distance x and $f(r/r_w)$ is the similarity function. Experimental data (Naudascher [15]) confirm the prediction, showing that this region is independent of both geometry and problem configuration.

The *near wake region* ($x/B < 7$), on the other hand, is characterised by a motion field that is strongly dependent on rotor and hull geometry. In this area, the highest SL concentrations are present and several analyses have already been conducted on this specific topic (Copercini [14]). In this project, however, LES simulations were carried out taking into account the ship's hull, propeller rotation, and the distribution of reactive calcium hydroxide. Thanks to the use of OpenFOAM, an open-source CFD simulation software, several reactive and non-reactive simulations of the neighbouring wake region were performed in order to assess the chemistry of the problem. Different input concentrations of $Ca(OH)_2$, with the same amount of discharge rates, will also be evaluated to check for differences and potential benefits or risks.

2 | Physical Model

The present chapter will present an overview of the physical aspects of the analysed problem. The first part will focus on the governing equations solved in fluid-dynamic, with particular attention to the adopted turbulence model. The second part will instead be dedicated to the chemical reactions encountered and how the coupling between chemistry and fluid dynamics is formulated.

2.1. Governing equations

This section will show the fluid-dynamics of the problem, that is to say Navier-Stokes equation, turbulence modeling and particularly Large Eddy Simulation as chosen method. Finally an insight into the Smagorinsky model will be presented.

2.1.1. Navier-Stokes Equation

The fluid dynamic system is represented by the incompressible Navier-Stokes equation for Newtonian flow. The equations, written in Cartesian coordinate system, result:

- Continuity equation:

$$\frac{\partial u_i}{\partial x_i} = 0 \tag{2.1}$$

- Momentum equation:

$$\frac{\partial u_i}{\partial t} + \frac{\partial}{\partial x_i}(u_i u_j) = -\frac{1}{\rho}\frac{\partial p}{\partial x_i} + \nu \frac{\partial}{\partial x_i}(\frac{\partial u_i}{\partial x_j} + \frac{\partial u_j}{\partial x_i}) \tag{2.2}$$

where ν is the constant kinematic viscosity, $\mathbf{x} = [x_1, x_2, x_3]$ is the coordinate vector and $\mathbf{u} = [u_1, u_2, u_3]$ is the velocity vector.

2.2. Turbulence modeling and LES approach

In order to solve (2.1) and (2.2), numerical simulations are required. Computational Fluid Dynamics (CFD) is the study of fluid motion by numerical simulation, where the basic idea is to use appropriate algorithms to find solutions to the equations describing the fluid motion. Solving the unsteady Navier-Stokes equations implies that we must take into account all the space-time scales of the solution if we want to have a result of maximum quality. The discretization, in space and time, has to be fine enough to represent the characteristic length and time associated with the smallest dynamically active scale of the exact solution. Turbulent flows are really complex problem due to the presence of scales of different sizes. By taking the case of statistically homogeneous and isotropic turbulent flow, we can observe that the ratio between the characteristic length of the most energetic scale, L, and that of the smallest dynamically active scale, η, is evaluated by the relation:

$$\frac{L}{\eta} = O(Re^{3/4}) \tag{2.3}$$

in which Re is the Reynolds number, defined as ratio between inertial and molecular viscosity effects. In order to obtain a complete solution over time, in a volume equal to L^3, we would need to solve the equations $O(Re^3)$ times. With current computational resources, this is an unreachable goal for problems with very high Reynolds number, like in aeronautical applications, where $Re \approx 10^8$. With these premises, three approaches can be adopted:

- Direct Numerical Simulation (DNS). All the space-time scales of the flow are resolved. This is a very demanding technique that can be performed only for cases with low Reynolds and simple geometries;
- Reynolds Averaged Navier Stokes (RANS). An ensemble average filter is applied to the exact solution $\boldsymbol{u}$, thus splitting it into the sum of its statistical average $< \boldsymbol{u} >$ and a fluctuation $\boldsymbol{u'}$. This is used to solve most of the engineering problems;
- Large Eddy Simulation (LES). The largest turbulent scales contains the majority of energy and anisotropy. With this approach, scales are fully resolved up to a certain point, while the residual energy, hence scales, is modelled (Figure 2.1. From a computational point of view, LES simulations are an optimal tradeoff between accuracy of DNS and low computational cost of RANS.

At high Re, according to Kolmogorov's theory, the scale separation increases as pointed out by equation (2.3), and throughout the energy cascade process there is a memory loss of the large eddies, with return to local isotropy (Pope [24]). With LES simulation, as al-

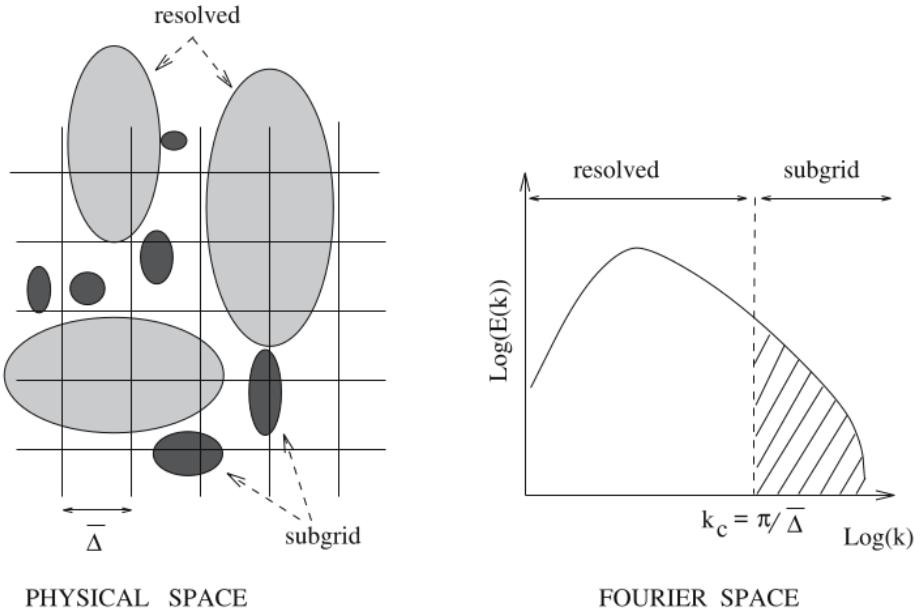

Figure 2.1: A simple scheme of filtering operation in both spatial and Fourier space: structures greater than $\overline{\Delta}$ (left), or with wavenumber less than k_c (right), are resolved. Taken from Sagaut [21] p. 11

ready introduced above, it's possible to capture large scales of motions with a satisfactory accuracy. The steps for this kind of approach are:

- **Decomposition**: the solution is splitted into large and small-scale components;
- **Filtering**: a filter (in physical or spectral domain), is applied to NS equations;
- **Closure**: unresolved scales are modeled with dedicated turbulence models;
- **Solution**: filtered NS equations are resolved.

The following is a discussion of how the various steps are implemented.

2.2.1. Filtering and Closure steps

For the sake of clarity, the operation of filtering will be presented only for an homogeneous low-pass filter, i.e *isotropic*[1]. This means that its properties are independent of the position and orientation of the frame of reference in space, which implies that it is applied to an unbounded domain and the cutoff scale[2] is constant and identical in all directions of space. The first step consists in splitting the exact solution $\phi(\mathbf{x}, t)$ into a filtered $\overline{\phi}(\mathbf{x}, t)$

[1]For more details about anisotropic filters, see [21]
[2]For cutoff scale, we intend the smallest scale resolved

and a residual contribute $\phi'(\mathbf{x},t)$.

$$\phi(\mathbf{x},t) = \overline{\phi}(\mathbf{x},t) + \phi'(\mathbf{x},t) \tag{2.4}$$

The filtered solution $\overline{\phi}(\mathbf{x},t)$ is characterised by a convolution product as:

$$\overline{\phi}(\mathbf{x},t) = \int\int_{-\infty}^{\infty} \phi(\boldsymbol{\xi},t) G(\boldsymbol{x}-\boldsymbol{\xi}, t-t') dt' d^3\boldsymbol{\xi} \tag{2.5}$$

where G is the Kernel of the filter. The dual definition in the Fourier space, which is a much more convenient way of dealing with turbulence scales, is obtained by multiplying the spectrum $\hat{\phi}(\boldsymbol{k},\omega)$ of $\phi(\mathbf{x},t)$ by the spectrum $\hat{G}(\boldsymbol{k},\omega)$ of the kernel $G(\boldsymbol{x},t)$:

$$\hat{\overline{\phi}}(\boldsymbol{k},\omega) = \hat{\phi}(\boldsymbol{k},\omega)\hat{G}(\boldsymbol{k},\omega) \tag{2.6}$$

where k and ω are the spatial wave number and time frequency, respectively. The function $\hat{G}$ is the transfer function associated with the kernel G. The spatial cutoff length $\overline{\Delta}$[3] is associated with the cutoff wave number k_c and time $\overline{\tau_c}$ with the cutoff frequency ω_c. The second term, referring to (2.4), is the residual solution, obtained as:

$$\phi'(\mathbf{x},t) = \phi(\mathbf{x},t) - \int\int_{-\infty}^{\infty} \phi(\boldsymbol{\xi},t) G(\boldsymbol{x}-\boldsymbol{\xi}, t-t') dt' d^3\boldsymbol{\xi} \tag{2.7}$$

An important feature of the residual term that should be emphasised is that it is not a deterministic variable, so:

$$\overline{\overline{\phi}}(\boldsymbol{x},t) \neq \overline{\phi}(\boldsymbol{x},t) \qquad \overline{\phi'}(\boldsymbol{x},t) \neq 0 \tag{2.8}$$

Different convolution filters can be adopted at this stage. The most common ones are:

- Box Filter:

$$G(x-\xi) = \begin{cases} \dfrac{1}{\overline{\Delta}} & \text{if } |x-\xi| \leq \dfrac{\overline{\Delta}}{2} \\ 0 & \text{otherwise} \end{cases}, \tag{2.9}$$

  This filter is local in the physical space and non-local in the Fourier space. This is also said to be smooth because there is a frequency overlap between the quantities

[3] In a three-dimensional, anisotropic case the filter has three different cut-off scales in space for each direction of the selected reference frame ($\Delta_1\Delta_3\Delta_3$), and the bandwidth is straightfully defined ad $\overline{(\Delta)} = (\Delta_1\Delta_3\Delta_3)^{1/3}$. It should be noted, however, as can be seen later, that in the case of a non-homogeneous filter it is not possible to switch the filtering operation with that of the derivative.

$\overline{\mathbf{u}}$ and $\mathbf{u}'$.

- Gaussian filter:

$$G(x-\xi) = (\frac{\gamma}{\pi\overline{\Delta}^2})^{1/2} exp\left(\frac{-\gamma|x-\xi|^2}{\overline{\Delta}^2}\right) \tag{2.10}$$

  This filter is smooth and non-local both in the spectral and physical spaces.

- Spectral or sharp cutoff filter:

$$G(x-\xi) = \frac{sin(k_c(x-\xi))}{k_c(x-\xi)}, \text{ with } k_c = \frac{\pi}{\overline{\Delta}} \tag{2.11}$$

  This filter is local in the spectral space and non-local in physical space, inversely from the box filter. Plots of the different filters are presented in Figure 2.2.

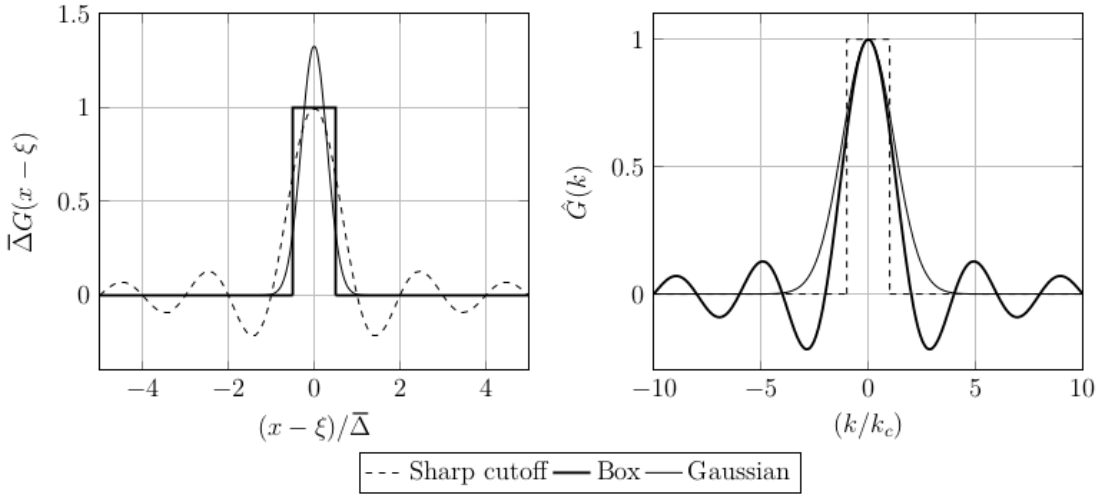

Figure 2.2: Filters convolution Kernel in physical(left) and spectral(right) spaces

Once defined the filter adopted, which in the present work is a box filter, this has to be applied to NS equations obtaining:

$$\frac{\partial \overline{u_i}}{\partial x_i} = 0 \tag{2.12}$$

$$\frac{\partial \overline{u_j}}{\partial t} + \frac{\partial}{\partial x_j}(\overline{u_i u_j}) = -\frac{1}{\rho}\frac{\partial \overline{p}}{\partial x_i} + \nu \frac{\partial^2 \overline{u_j}}{\partial x_i \partial x_j}, \tag{2.13}$$

where the term $\overline{u_i u_j}$ can be decomposed (Germano [10]) as:

$$\overline{u_i u_j} = \tau_{ij}^R + \overline{u}_i \overline{u}_j \tag{2.14}$$

The term τ_{ij}^R is called tensor of residual stresses, also defined as Subgrid Scale (SGS) tensor, and it represents the interactions between the resolved and unresolved scaled.

The SGS tensor can be further broken down into:

$$\tau_{ij}^R = \tau_{ij}^r + \frac{2}{3}k^R\delta_{ij} \tag{2.15}$$

with δ_{ij} being the Kronecker's delta and k^R the kinetic energy of residual motions, which can be included in the isotropic contribution of stress tensor $\overline{p'} = \overline{p} - 2/3rhok^R$. The anisotropic component of the residual stresses tensor τ_{ij}^r is the element that gives rise to the closure problem. In fact, the new filtered momentum equation is:

$$\frac{\partial\overline{u_j}}{\partial t} + \overline{u_i}\frac{\partial\overline{u_j}}{\partial x_i} = -\frac{1}{\rho}\frac{\partial\overline{p}}{\partial x_j} + \nu\frac{\partial^2\overline{u_j}}{\partial x_i\partial x_j} - \frac{\partial\tau_{ij}^r}{\partial x_i}, \tag{2.16}$$

The closure problem can be solved by modelling the only unknown term, i.e. τ_{ij}^r.

2.2.2. The Smagorinsky Model

The Smagorinsky [23] model provides a solution to closure for filtered equation. It's a physical model that relies upon the hypothesis of subgrid viscosity. The assumption is that the subgrid stress tensor τ_{ij}^r has the same mathematical structure as a molecular diffusion term. That is to say, a subgrid viscosity ν_{sgs} have to be introduced in order to respect the hypothesis[4]. This last step implies that the smallest scale behaviour is analogous to the Brownian motion of the molecules (Sagaut [21]). Boussinesq was the first to develop this concept in the following form:

$$\tau_{ij}^r = -2\nu_{sgs}\overline{S}_{ij} \tag{2.17}$$

$$\overline{S}_{ij} = \frac{1}{2}\left(\frac{\partial\overline{u}_i}{\partial x_j} + \frac{\partial\overline{u}_j}{\partial x_i}\right) \tag{2.18}$$

with $\overline{S}_{ij}$ defined as the strain rate tensor. The Boussinesq formulation holds upon the hypothesis of alignment of the eigenvectors of the strain rate tensor and the subgrid tensor. This is partially incorrect for turbulent flows, since there is no clear separation between scales. This hypothesis can be justified in the inertial subrange of homogeneous isotropic turbulence at high Re.
Moving on, at this point the subgrid viscosity can be expressed as a function of a Smagorin-

[4]In this case, it's important to notice that this fictitious viscosity is a property of the flow and not of the fluid

sky characteristic length l_s, analogous to the mixing length theory[5]:

$$\nu_{sgs} = l_s^2 \overline{S}_{ij} = (C_s \Delta)^2 \overline{S}_{ij} \tag{2.19}$$

where Δ is the filter width and C_s the Smagorinsky constant. This quantity is not universal, and for isotropic homogeneous turbulence in channel flow it usually oscillates between 0.1 and 0.2, depending on the case.
It's convenient to make a few consideration about the model adopted. It's already clear from the beginning that the Smagorinsky model relies upon partially wrong hypothesis, but it also shows some limits in representing the energy cascade and the interactions between resolved and subgrid scales. In a turbulent flow, there is a large departure from the local equilibrium, because the turbulent timescale is larger than the shear timescale, causing the subgrid stresses to have a memory of the shear flow. The problem could be solved adopting a non-linear relation between the residual stress tensor and the strain-rate tensor, in which the memory process is introduced. The Smagorinsky model, according to (2.17), also express the dissipation energy as [24]:

$$\epsilon_r = -\tau_{ij}^r \overline{S}_{ij} = 2\nu_{sgs} \overline{S}_{ij} \overline{S}_{ij} = \nu_{sgs} \overline{S}^2 > 0 \tag{2.20}$$

Thus, for the Smagorinsky model, energy transfer occurs everywhere from filtered to residual motions: there is no backscatter.
Many improved subgrid models have been developed such as the dynamic Germano model [10], in which the C_s parameter is not a constant, but it is locally computed and adjusted in relation to the flow behaviour. It is worth noticing that the latter are more computationally demanding rather than the Smagorinsky model. Although the limits explained in the last chapter, the extensive use of the Smagorinsky model in recent decades, due to its satisfactory accuracy in high Re flows and its low computational cost, makes it a suitable candidate for this project.

2.3. Conservation equations for reacting fows

This section is devoted to briefly showing how governing equations presented in section 2.1 need to be modified when dealing with reacting flows. Hence, a general definition of a reacting flow is given, then moving to a presentation of the conservation and constitutive equations for such flows. Finally, some basic notions about chemistry related to the project

[5]The mixing length model is a method attempting to describe momentum transfer by turbulence Reynolds stresses within a Newtonian fluid boundary layer by means of an eddy viscosity. It has been developed by Prandtl [20] in 1925.

will be provided, in order to create a closed model that can be used by the numerical code, fully explained in chapter 3.

2.3.1. Definition of reacting flow

The problem at hand confronts us with a stream composed of multiple species that must be followed individually in order to obtain meaningful data. Each species has specific thermodynamic ($e,\ h,\ p,\ T,\ s$ ...) and transport properties (μ and k), which may vary with temperature and concentration in space. During the simulation, species react chemically and reaction rates require specific modelling. Moreover, for each component of the mixture, transport coefficients (heat diffusivity, species diffusion, viscosity, etc...) require specific care.

2.3.2. Chemical mechanism

In the present work the Penner's formalism will be adopted, expressing a generic chemical equations between species A, B, C as:

$$A + B \leftrightarrow C \tag{2.21}$$

$$\sum_{i=0}^{n} \nu_i' M_i \leftrightarrow \sum_{i=0}^{n} \nu_i'' M_i \tag{2.22}$$

where ν_i is the i^{th} stoichiometric coefficient respectively for reactants (ν_i') and products (ν_i'') and M_i is the i^{th} chemical specie of mixture. These equations are sufficient only for problems in chemical equilibrium, where the reaction rates are infinitely fast and, for a given thermodynamic state, the equilibrium composition of the mixture is uniquely determined. From previous studies (Abbate and Bianchi [2]), it is reasonable to assume that the typical reaction time for the dissociation of slaked lime is comparable with respect to mixing characteristic time of the propeller induced motion, hence requiring the formulation of a chemical kinetic. This is usually expressed, given an elementary reaction as (2.21):

$$\frac{d[A]}{dt} = \frac{d[B]}{dt} = -k_1[A][B] \tag{2.23}$$

$$\frac{d[C]}{dt} = k_1[A][B] \tag{2.24}$$

where the quantities between brackets are the concentrations of each specie and k_1 is the rate constant that describes how fast is the production of chemical products. Species are characterized through their mass fractions Y_k ($k = [1, N]$, where N is the number of

species in the reacting mixture.

$$Y_k = \frac{m_k}{m} \tag{2.25}$$

with m_k mass of the single specie and m total mass of the mixture. These equations require the definition of the k_1 term, which in this work is given by the Arrhenius law, that express the rate constant as a function of temperature only. In OpenFOAM source files, this is expressed as:

$$k = A * T^{\beta} exp^{(-\frac{T_a}{T})} \tag{2.26}$$

with A being the pre-exponent factor, T_a the activation temperature and β the constant exponent of the temperature in the calculation of the reaction rate. All the constants can be tuned in order to obtain the desired chemical behaviour, as it will be seen in section 5.1. These relationships create a set of Ordinary Differential Equations (ODEs), function of number of species, and dependent on number of reactions. For the present work, the actual chemical reaction occurring in the ocean is actually a chain of multiple reactions, as can be seen in sections 1.1.1 and 1.2. However, for comparisons with previous works [Caserini [4], Abbate and Bianchi [2]], and for computational costs, only the dissolution of the slaked lime will be simulated, thus neglecting the whole carbon cycle.

$$Ca(OH)_2 \leftrightarrow Ca^{2+} + 2OH^- \tag{2.27}$$

2.3.3. Governing equations for reacting flows

Given the equations in section 2.3.2, two more aspects needs to be furtherly inspected:

- thermodynamic and transport properties of the mixture;
- NS equations.

Regarding constitutive equations of thermodynamic and transport properties, constant values or other modeling functions must be provided to the set of equations. Regarding the NS equations for a reacting mixture, the momentum equation doesn't formally change between a reacting and a non reacting case [Poinsot [19]]. The energy equation, for the sake of clarity, won't be shown given the low contribution to the reaction and the project's lack of interest in investigating thermodynamic quantities, since the temperature does not vary during the chemical reaction. The single specie mass conservation equation is expressed as:

$$\frac{\partial(\rho Y_k)}{\partial t} + \frac{\partial}{\partial x_i}(\rho(u_i + V_{k,i})Y_k) = \dot{\omega}_k \ for \ k = 1, N \tag{2.28}$$

where $V_{k,i}$ is the i-component of the diffusion velocity V_k of species k and $\dot{\omega}_k$ is the reaction rate of species k. By definition:

$$\sum_{k=1}^{N} Y_k V_{k,i} = 0 \ and \ \sum_{k=1}^{N} \dot{\omega}_k = 0 \tag{2.29}$$

At this point, two contributes must be defined:

- the diffusion velocities, which is always a problem on itself, require, for the most accurate solution possible, the resolution of a linear system of size N^2 in each direction at each point and at each instant, for unsteady flows. This is a difficult and expensive task that can be simplified with models like the Fick's law or the Hirschfelder and Curtiss approximation. The Fick's law it's the model adopted in this project. The approximation fixes the diffusion coefficient D required for the computation of diffusion velocities. The equation can be expressed like:

$$V_k = -D\nabla Y_k \tag{2.30}$$

- the source term $\dot{\omega}_k$, which is related to the specific rate k via:

$$\dot{\omega} = k\Pi_{i=1}^{N}[M_i]^{\nu_i'} \tag{2.31}$$

3 | Numerical Model

The chapter presents an overview of how the equations presented above are solved by the code. The software adopted is OpenFOAM-9 [16], an open-source tool that comes with a great variety of solvers for different applications. The present chapter is subdivided in two main sections:

- a brief presentation of the resolution mechanism of the solver adopted will be explained, focusing on how the chemical equations of the previous chapter are approached and solved;
- an explanation of how the mesh is generated and put in motion through the Multiple Reference Frame approach.

3.1. reactingFOAM solver

OpenFOAM makes use of the Finite Volume method, that uses the integral form of the conservation equations as its starting point. The solution domain is subdivided into a finite number of contiguous control volumes (CVs), and the conservation equations are applied to each CV. At the centroid of each CV lies a computational node where the variable values are to be calculated. This method can deal any type of grid, making it a suitable approach for complex geometries. Both domain and equations have to be discretized in time and space with sufficient order of accuracy. In general, methods of order higher than second are very difficult to develop in 3D cases, due to the fact that FV approach requires three levels of approximation: interpolation, differentiation and integration.
The discretization operation for each conservation equation leads to a system of linear equations that needs to be solved. Repeating the process for each cell creates a linear system of equations that has to be solved in the most convenient way, i.e. iteratively, given the dimension and the complexity of the 3D geometry adopted. All these steps (discretization in space and time, discretization of equations, solution algorithms for each quantity) can be customized inside the OpenFOAM environment.

3.1.1. Segregated solver

The problem to be solved consists in a coupled systems of equation, since some quantities, like velocity vector, pressure or density, are present in more than one equation. It has to be pointed out that the finite-volume method solves for ρu, a conservative variable. This explains the formulation of the next equations. There are two types of approaches to such problems:

- **simultaneous methods**, also called **coupled solvers**, where all variables are solved for simultaneously;
- **sequential methods**, also called **segregated solvers**, where each equation is solved for its dominant variable, treating the other variables as known, and one iterates through the equations until the solution of the coupled system is obtained.

The specific solver used (*reactingFOAM*) is a segregated one, and the algorithm that dictates how to solve the system is called PIMPLE, which is a derivation of the base algorithm SIMPLE (Semi-Implicit Method for Pressure Linked Equations). The acronym PIMPLE comes from the union of PISO algorithm name (Pressure-Implicit with Splitting of Operators), another unsteady algorithm for the resolution of NS equations, and SIMPLE algorithm.
In the incompressible case, the solution of the Navier-Stokes equations (2.2) and (2.1) is complicated by the lack of an independent equation for the pressure, whose gradient contributes to each of the three components of the momentum equation. From this point of view, the mass conservation is more like a kinematic constraint on the velocity field rather than a dynamic equation. One way out of this difficulty is to construct the pressure field so as to guarantee satisfaction of the continuity equation. The method adopted for this problem is called Projection Method, proposed by Chorin [5], and it's basically a fractional step method where:

- an intermediate velocity u^* is computed, explicitly using the momentum equation by ignoring the pressure gradient term.

$$\left.\frac{\partial(\rho u_i)}{\partial t}\right|_n^* = \left(-\frac{\partial(\rho u_i u_j)^{n+1}}{\partial x_i} + \frac{\partial \tau_{ij}^{n+1}}{\partial x_j}\right) \tag{3.1}$$

  where n and $n+1$ are respectively the previous and current step of the iterative simulations.

- in the second half step, called the *projection step*, the pressure gradient is used to

correct the provisional momentum $(\rho u_i)*$ following the relation:

$$\left.\frac{\partial(\rho u_i)}{\partial t}\right|_{*}^{n+1} = -\nabla p^{n+1} \tag{3.2}$$

obtaining the correct solution $(\rho u_i)^{n+1}$.

- computing the right hand side of the equation (3.2) requires the knowledge of the pressure at the next step, and this can be obtained by calculating the divergence of the projection step and combining it with the continuity equation, thus deriving the Helmoltz equation:

$$\nabla^2 p^{n+1} = \frac{1}{\Delta t}\left[\frac{\partial(\rho)}{\partial t} + \nabla \cdot (\rho^* u^*)\right] \tag{3.3}$$

The velocity field is now forced to satisfy a discrete continuity constraint at the end of each time step.

3.1.2. PIMPLE algorithm

Here, a brief overview of the algorithm is reported, for a compressible flow , with all the aspects that need to be accounted for the actual project, that means including chemistry and also energy equation, even if we are not interested in thermodynamic quantities. The model presented is the most general possible, thus it take into accounts different aspects that are beyond the scope of the thesis, like enthalpy or temperature. As visible from Figure 3.1:

- first, after some preliminary calculations regarding mesh motion (as in our case with the propeller), the momentum equation is computed returning a guess velocity field;
- next, energy equation is solved: this is an essential step for the introduction of source term related to heat transfer, combustion phenomena or, more in general, chemistry;
- now, the Helmoltz equation for the pressure is solved through an iterative process, and the velocity field is corrected imposing the solenoidal constraint;
- the turbulent viscosity, out of the inner loop, is updated and the new velocity field can be used to solve the momentum equation once again, repeating the outer loop.

PIMPLE algorithm differs from SIMPLE and PISO because it can deal with transient simulations, while SIMPLE can not, and merges the controls of PISO and SIMPLE (hence the merged acronym). In particular, it can perform inner and outer loops (Figure 3.1)

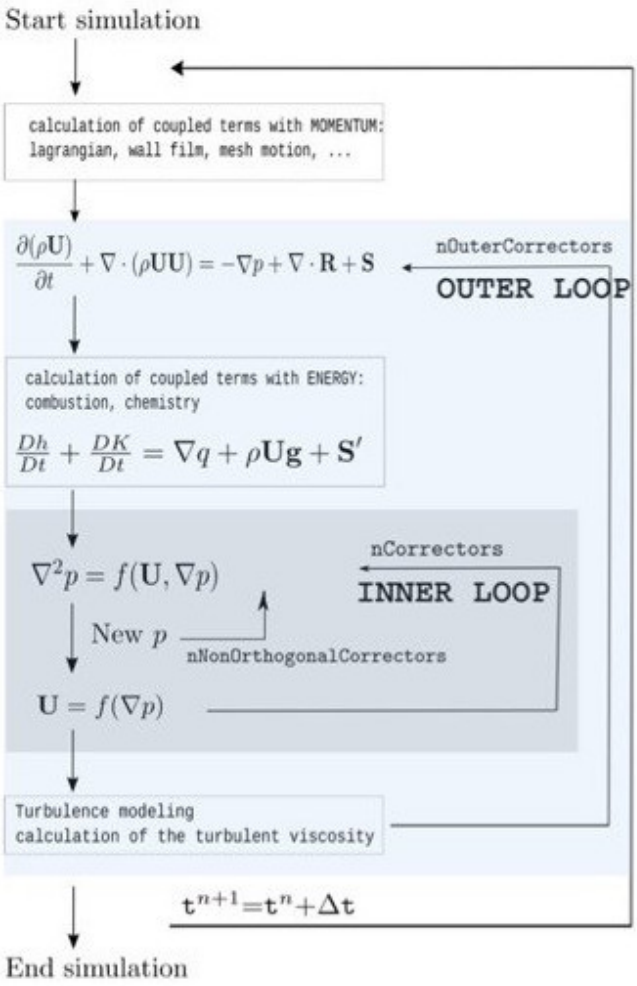

Figure 3.1: A simplified scheme of the steps performed by the solver at each time step: note the inner and outer loops present in any segregated solver. Courtesy of professor F.Piscaglia.

as many times as wanted, with an obvious increase in computational time, to obtain a better convergence. When the cycle ends, current results are used as a basis for the next time step. For the PISO algorithm, the pressure is corrected twice while the momentum is corrected once. For the SIMPLE algorithm, the outer loops can be freely selected and the pressure correction is performed only once.
Regarding the present work, two inner corrections and two outer ones are performed, in order to find a reasonable compromise between accuracy and computational cost.

3.1.3. Describing the kinetic chemistry

As explained in section 2.3.2, the equations to be solved are ODEs that requires a significant smaller timestep in order to be solved precisely. That means that ODEs must be solved for a number of chemical subtimesteps for every fluid dynamic timestep. This is necessary in order to obtain source terms, while preserving mass conservation. A simplified list of steps can be shown:

- ODEs are solved for all chemical subtimestep until the next fluid dynamic timestep. This is done, in the present work, by using the *seulex* implicit method. Seulex solver is optimal with high number of cells, allowing a small number of chemical timesteps per fluid dynamic ones;
- source terms, like $\dot{\omega}$, are calculated using the results from the previous step;
- such terms are inserted into the species equations (2.28) while preserving continuity;
- the process is repeated for every fluid dynamic timestep. Each chemical subiteration is solved when a tolerance constraint is reached.

Whenever chemistry is accounted in OpenFOAM, computational time and cost necessarily increase, due to a more complex set of equations and a smaller chemical subtimestep. Also, OpenFOAM executes a serial process while simulating, thus calculating the solution of once cell at time. This numerical problem is partially solved by creating different "*if statement control*" applied on chemical reactions. The discrepancy between the timesteps can also be treated using the *Local Time Stepping* (LTS), as in the present work, in which the time step is manipulated for each individual cell in the mesh, making it as high as possible in order to reduce computational costs. It then processes the time-step field by smoothing the variation in time step across the domain to prevent instability due to large conservation errors caused by sudden changes in time step.
The last feature about the solver adopted that must be explained is how the source terms, like $\dot{\omega}$ are computed. In fact, for a proper simulation of a simple chemical reaction, all the intermediate steps of the chemical process, all transport equations and all flow equations have to be satisfied simultaneously. All these factors have a significant effect on the computational speed and time of the simulation, but with proper simplifying assumptions this can be done without substantial compromise on the accuracy and convergence of the solution. The discriminating quantity between the models that can be adopted is the Damköler number, which expresses the ratio between the characteristic diffusion and reaction time.

$$Da = \frac{\text{diffusion time}}{\text{reaction time}} = \frac{\text{reaction rate}}{\text{convective mass transport}} \tag{3.4}$$

Thus, if $Da >> 1$, the chemical reactions are supposed to be much faster than turbulent phenomena, so that the reaction rate can be controlled only by mixing, and therefore leading to an infinitely fast chemistry model. Otherwhise, a finite-rate chemistry model has to be adopted. For the present work, since mixing and turbulent effects need to be taken into account, the Partially Stirred Reactor model (PaSR) [16], which is a finite-rate model, will be used the code for the solution.
With this model, the reaction rate is corrected by the chemistry solver with a reaction limiter k:

$$R_i = k\dot{\omega}_{i,chem} \tag{3.5}$$

The reaction limiter is computed based on the mixing time scale:

$$\tau_k = C_{mix}\sqrt{\frac{\nu}{\epsilon}} \tag{3.6}$$

$$k = \begin{cases} \dfrac{\tau_{chem}}{\tau_{chem} + \tau_k} & \text{if } \tau_k > 0 \\ 1 & \text{otherwise} \end{cases}, \tag{3.7}$$

where ν is the kinematic viscosity and ϵ represents the dissipation rate, while C_{mix} is a constant that can be tuned if needed.

3.2. Multiple Reference Frame (MRF)

In order to simulate the propeller motion, OpenFOAM allows to model rotating elements in two main ways:

- by actually moving the mesh, modifying it at each iteration. This method is called sliding mesh and can provide very accurate results in the proximity of the propeller's surface, but it's computationally expensive, since smaller time steps are required in order to obtain an accurate and stable solution;
- by defining multiple reference frames, which implies solving the equations for the motion of the propeller in a reference frame that moves with the rotating part itself.

The MRF approach will be adopted for this project, because it comes with different advantages. In order to solve the problem, it's necessary to add source terms to momentum equation (2.2). By defining a second reference frame that moves with the rotating part itself, the source terms are solved using a stationary model, thus significantly reducing the computational cost. In a nutshell, referring to a reference system which moves along with the propeller's blade, a global velocity $\boldsymbol{U}$ and an inertial velocity $\boldsymbol{U_r}$ are defined,

together with a rotation vector $\boldsymbol{\Omega}$, a velocity triangle can be visualised in Figure 3.2.

$$\boldsymbol{U} = \boldsymbol{U_r} + \boldsymbol{\Omega} \times \boldsymbol{r} \tag{3.8}$$

where $\boldsymbol{r}$ is the distance from the rotation axis.

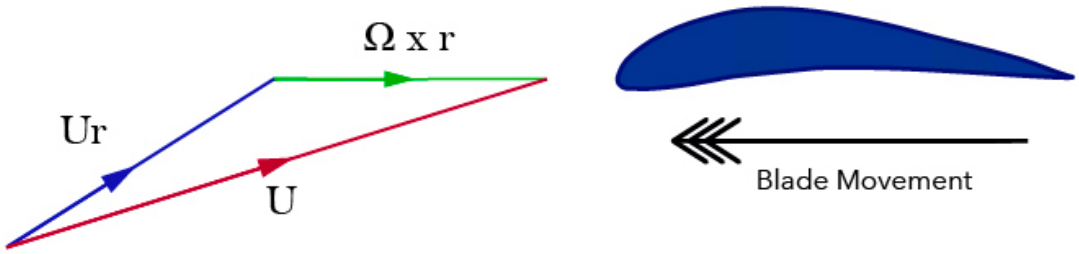

Figure 3.2: Triangle of velocities in a blade's reference frame. $\boldsymbol{U}$ is the global velocity, $\boldsymbol{U_r}$ the relative velocity, $\boldsymbol{\Omega}$ the rotation vector, $\boldsymbol{r}$ distance vector.

From eq (3.8), steady Navier-Stokes equations can be rearranged[1] with the new formulation of the global velocity, thus obtaining:

$$\underbrace{\nabla \cdot (\boldsymbol{U}\boldsymbol{U_r})}_{\text{convection term}} = -\nabla p + \nabla \cdot (\nu \nabla \boldsymbol{U}) - \underbrace{\boldsymbol{\Omega} \times \boldsymbol{U}}_{\text{source term}} \tag{3.9}$$

The main problem now is the convective term, which contains both the global velocity and the relative one. In a finite volume workframe, this means that the face volume flux contains the $\boldsymbol{U_r}$ too. By substituting again $\boldsymbol{U_r}$ with eq. (3.8), a second source term can be obtained, representing a **face** (or volume) **flux correction**. This is evaluated for all the faces in the rotating zone.

[1] For the complete derivation, refer to [17]

4 | Fluid-dynamic simulations

This paragraph is devoted to the discussion and presentation of results of the simulations performed. So far, the underlying tools adopted for the present work have been explained and discussed, both for the physical model encountered and the computational methods required. When complex simulations are performed, it's always useful, for a good convergence and a good initialization of the problem, to execute preliminary, simpler simulations. Particularly given the presence of a rotating element, it is mandatory that the final simulations begin with an already developed flow. Consequently, the steps leading to the final result are:

- a steady-state simulation using *simpleFoam* solver has been performed, with the propeller stopped;
- using the fields generated at the previous step, an unsteady simulation using *pimpleFoam* solver has been launched, with the propeller set in motion, without the injection of lime;
- from this point, the final simulation where the calcium hydroxide is injected, without chemical reactions, is performed.

This chapter is dedicated to the non reactive results, giving insights only regarding the fluid-dynamics aspects. Before presenting them, the geometry of the problem is reported. Next, a mesh convergence study has been performed, in order to ensure a good degree of confidence in the results, and their independence of the level of mesh refinement. For the sake of clarity, an overview of all the simulations will be presented after this paragraph, providing boundary conditions of interest and other setting parameters. For this project, supercomputer Galileo-100 from CINECA [7] has been used. The final simulations required the use of 3 nodes, totalling 144 cores, with an average simulation time of approximately 7 hours.

4.1. Geometry and Propeller Modeling

In Caserini's work [4], a Kriso container ship (KCS, length 232.5 m; width 32m; depth 19m; speed 8m/s [1]) is used for the discharge of slaked lime. This is due to the fact that this ship model is one of the most widespread one, therefore representing a valuable geometry for a real application of this process. An inlet for the lime discharge of diameter equal to $40cm$ is considered, positioned behind the propeller with Argentieri's thesis [9] as reference. The ship is modeled and analyzed in three dimensions and in full scale, defining the principal axis so that the length is aligned with the negative x axes, the width the y axis and the depth with the negative z axis. A complete simulation of the hull would be excessively detailed and it would not add relevant informations, since the prow of the ship poorly contributes to the ship's wake. This kind of simulation would also be excessively expensive in terms of computational resources. Hence, only the final portion of the hull will be considered. Considering that the study is focused on the near wake region and taking into account the strong mixing effect generated by the propeller, the free-surface can be neglected.

4.1.1. KP505 propeller

The propeller mounted on the KCS is the KP505, designed by the Korea Research Institute of Ships and Ocean Engineering. Nominal diameter is $7.9m$ and the principal particulars and open water characteristics[1] of the model are presented in Figures 4.1 and 4.2:

[1]The open water characteristics are provided as measurements in towing tank experiments from [13]

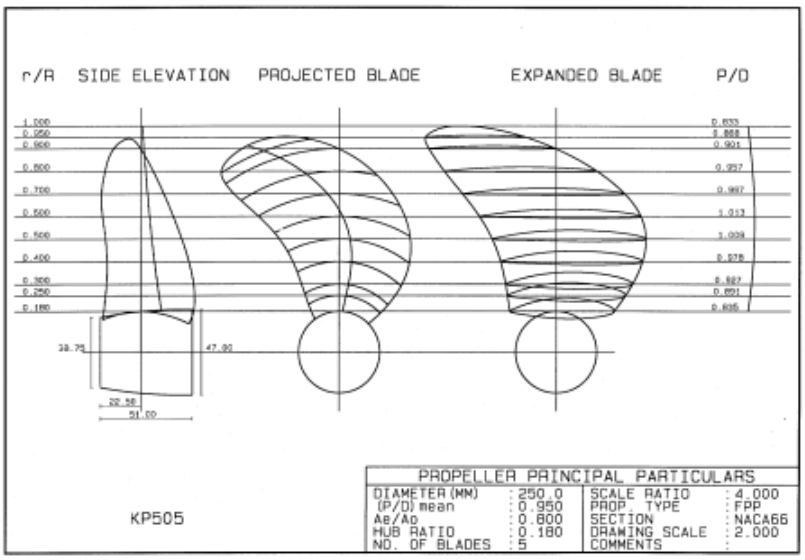

Figure 4.1: Propeller drawing with details

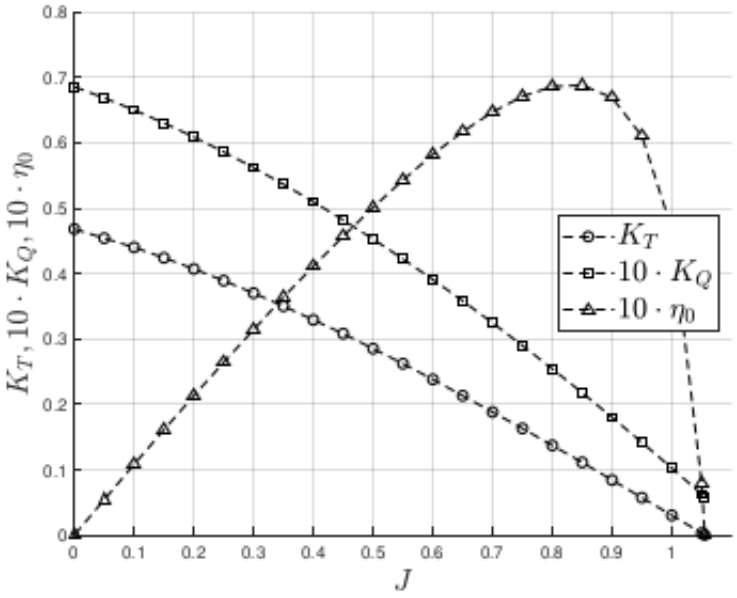

Figure 4.2: Open water data of the propeller, from [9]

The cruise velocity V_c of the container ship has been set to $8m/s$. In order to compute the rotational speed of the propeller n the advance ratio J is adopted. From Figure 4.2, in accordance with Argentieri's thesis [9], J can be set to 0.7. From the definition:

$$J = \frac{V_c}{n \cdot D} \tag{4.1}$$

with D diameter of the propeller. By inverting the formula the rotational speed can be retrieved:

$$n = \frac{V_c}{J \cdot D} = 1.44\ Hz = 9\ rad/s \tag{4.2}$$

4.1.2. Computational domain

The domain consists of a rectangular portion representing a region of ocean. The inlet section measures six diameters in width by four in height, while the length is eleven diameters. In addition, in Figures 4.3 and 4.4, it can be seen the *sphereEX* region, which is the portion of domain that will simulate the propeller rotation. This cylinder has a diameter of 6/5 the propeller's diameter and about $3/5D$ of depth. Dimensions of boundaries have been set in order to let the flow fully develop, without interference from boundary conditions. The propeller is located at about four diameters from the inlet. The mesh has been generated using the utilities `blockMesh` and `snappyHexMesh` from OpenFOAM mesh programs. First, an hexahedral domain is created with `blockMesh`, representing walls inlet and outlet, with referral to Figure 4.3. After this step, all the other elements are generated from `.stl` files with `snappyHexMesh`.

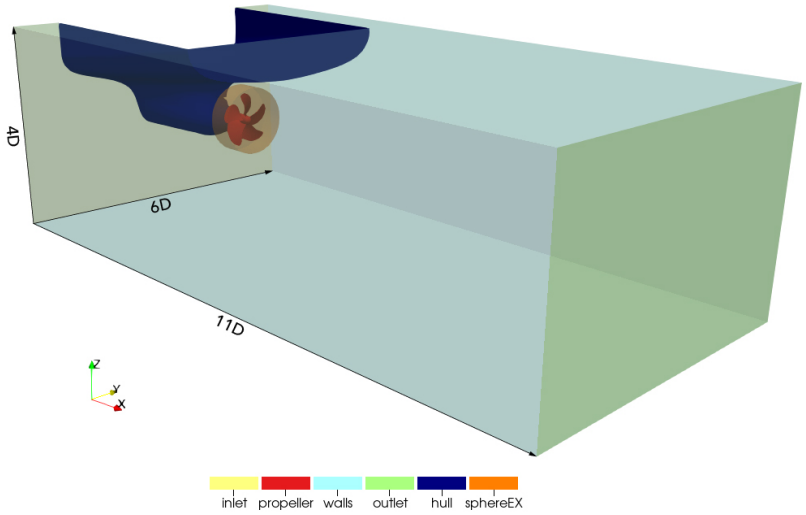

Figure 4.3: Domain boundaries with dimensions

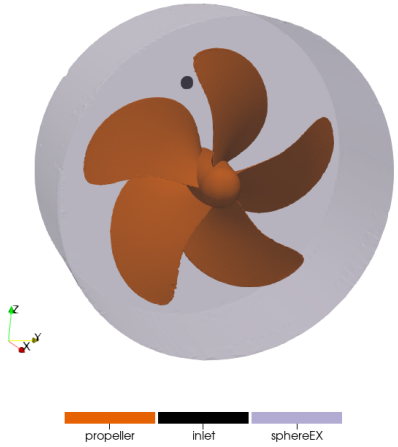

Figure 4.4: Propeller view with rotation region

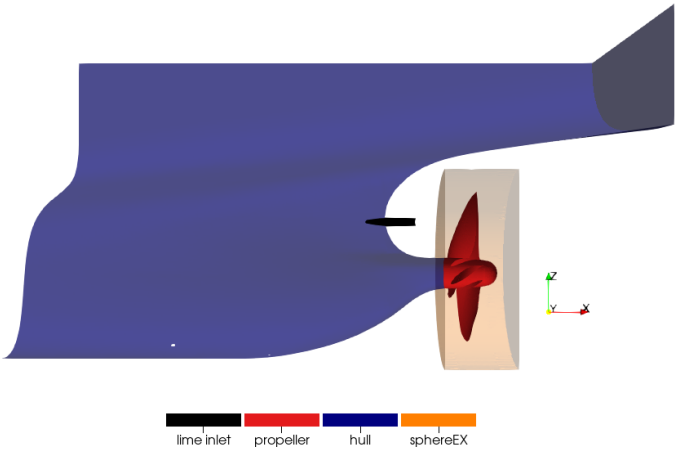

Figure 4.5: Slice of domain in the $y-$orthogonal direction

In Figure 4.5 the inlet from which the slaked lime is injected can be seen coloured in black. The inlet velocities and mass flow rates for this region of the domain are reported in section 4.3. Regarding other boundary and initial conditions, the walls and the outlet of the domain, referring to Figure 4.3, have been set to *zeroGradient*[2] for both velocity and pressure. For hull and propeller the velocity has been set to zero, in order to respect the non slip condition, while the inlet's velocity is 8 m/s along the $x-$axis. The same velocity has been set for the whole domain and for the *inletOutlet*[3] condition applied to the outlet patch.

[2] *zeroGradient* is a condition that sets the field to the internal field value.

[3] *inletOutlet* is a condition equal to the *zeroGradient* unless the flow is inward, in which case it becomes a fixed value equal to the one selected at the inlet.

A convergence study for the mesh has been performed in chapter 4.2. For the sake of clarity, the reference frame is defined with the $x-$axis oriented along the moving direction of the ship, while the $z-$axis points towards the water surface. Hence, the gravity vector in this project is defined as $\vec{g} = (0; 0; -9.81) m/s^2$.

4.2. Mesh convergence

Achieving a high level of accuracy in fluid-dynamic simulations requires refining the computational grid, which is commonly known as mesh convergence. It involves determining the minimum mesh size needed to obtain reliable and accurate results. The accuracy of the simulation is directly related to the resolution of the grid, making mesh convergence critical in fluid dynamics. It allows for the assessment of the impact of mesh quality on the accuracy of the results and ensures that they are independent of the mesh size used. Additionally, engineers and researchers can optimize computational resources and save time while still achieving accurate and reliable results by using mesh convergence. For this purpose, several simulations have been perfomed by keeping boundary conditions and solver adopted fixed, and changing only the mesh. In this particular context the structure of the mesh in question offers a difficult problem for the convergence study, as it presents a strong inhomogeneity in the refinement of the cells. In LES simulations, to resolve at least 80% of the turbulent kinetic energy, a very fine mesh is required, especially in areas where the velocity is highest and the turbulent effect most significant. As a result, two refinement zones have been introduced into the present mesh, one coinciding with *sphereEX*, a patch already introduced in chapter 3.2, and one in the ship's wake, as visible in Figures 4.6 and 4.7. Given these conditions, multiple meshes have been generated, in order to assess when the solution appears to be independent from mesh refinement. Each simulation lasted for 8 seconds, and the maximum Courant[4] number Co has been set to 0.9. To this purpose, the data provided by OpenFOAM for each mesh have been post-processed using MATLAB: along the x direction, different slices of domain were extracted and the maximum value was selected. After averaging over time, the results were plotted with respect to the length of the domain.
Given these premises, in Figure 4.8 the results of the analysis are shown. All cases show a speed peak due to the propeller thrust effect, followed by a progressive decrease within each slice, until a plateau speed is reached. The coarsest and finest meshes present a very similar behaviour, with the coarse one showing some peaks, probably due to mesh inconsistencies. Intermediate meshes, on the other hand, deviate from the previous trend,

[4]Courant number is a non-dimensional value that evaluates the time step Δt of a transient simulation given the mesh size Δx and flow velocity U through the equation $Co = \frac{U\Delta t}{\Delta x}$

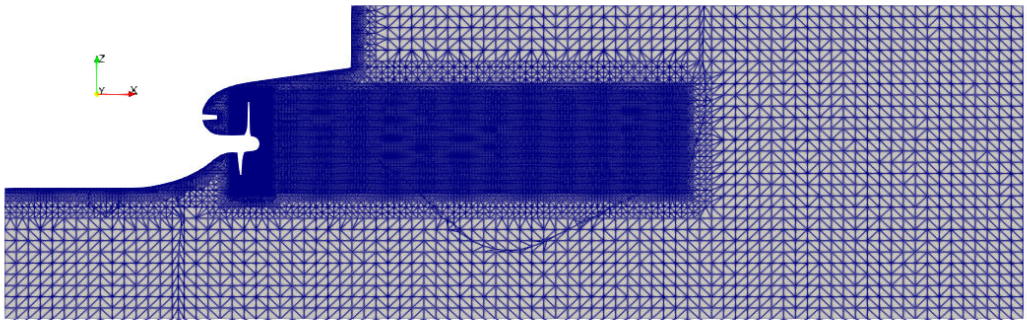

Figure 4.6: Lateral slice of the domain showing the refinement zones introduced, i.e. *sphereEX* and the wake zone.

but show a gradual rapprochement to the finer mesh if the resolution is increased. For this reason, the mesh used for the final simulations is the 16-million one.

4.3. Operative conditions

In order to analyze different conditions of injection, three cases are presented. For each one, a non reactive and a reactive simulation are performed, and in this chapter, only the former are presented. From Caserini et al. [4], a discharge of $CaOH_2$ equal to $\dot{m}_{CaOH_2} = 5\ Kg/s$ represents a desirable discharge flow of lime in order to obtain meaningful effects for the deacidification of seawater and CO_2 absorption. From this data, the flow rate of water emitted by the injector can be calculated as follows:

$$\dot{m}_{H_2O} = \frac{\dot{m}_{CaOH_2}}{Y_{CaOH_2}} \tag{4.3}$$

where Y_{CaOH_2} is the mass fraction of carbon hydroxide. Once the mass flow rate of water is computed, the velocity of the mixture injected from the lime inlet in Figure 4.5 is retrieved as:

$$U_{inlet} = \frac{\dot{m}_{H_2O}}{\rho A} \tag{4.4}$$

where A is the area of the inlet and ρ the sea water density. The concentrations adopted for the present work are:

- 2 g/l which is a low concentration case and presumably low risk that requires a lot of water, as visible from table 4.1;
- 20 g/l which is a limit for the chemistry model adopted, since it represents the satu-

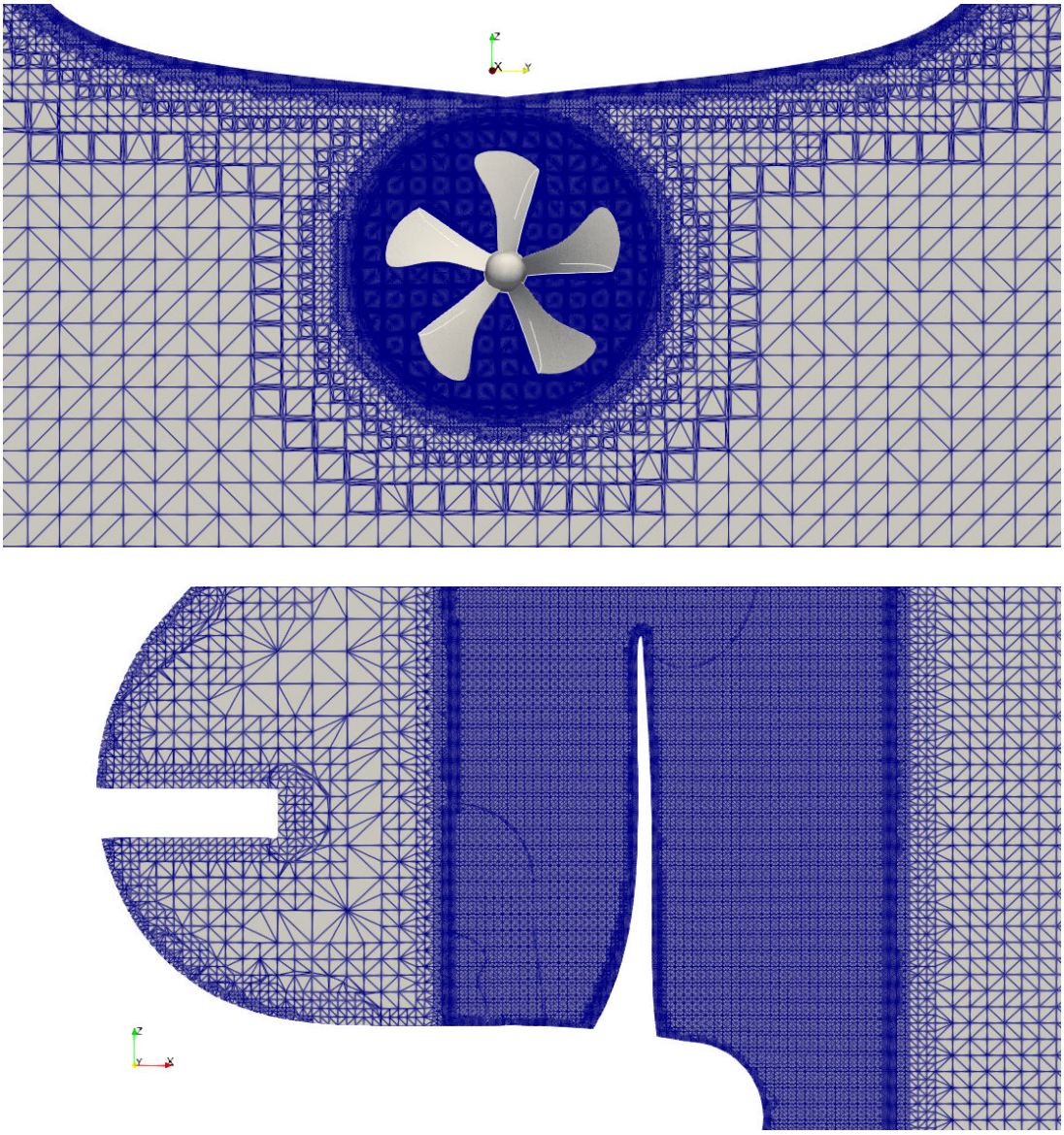

Figure 4.7: Top: a front view of the mesh grid around the propeller. Bottom: a detail of the grid between the propeller and the inlet.

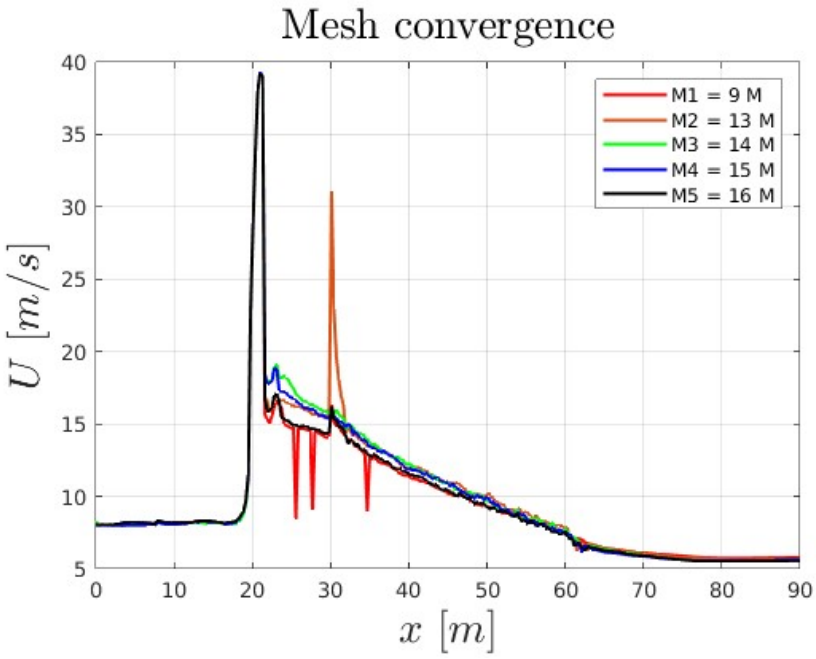

Figure 4.8: Plots of maximum velocity magnitude against x coordinate for different mesh sizes. The legend refers to the number of cells in millions.

ration limit of the solution. After this threshold, the slaked lime should be modeled as a particulate matter, thus requiring a lagrangian simulation, a much more expensive simulation that takes into account drag effects, interactions of particles with the fluid, evaporation...;

- 86.5 g/l which is the concentration adopted in Caserini's work [4]. The hypothesis of this test, based on the statements made above, are not completely satisfied, but a comparison seemed necessary.

In the following table the operative conditions explained above are summarised:

	2 g/l	20 g/l	86.5 g/l
Y_{CaOH_2} $[\frac{mol}{l}]$	0.027	0.273	1.169
$\dot{m}_{H_2O}$ $[\frac{l}{s}]$	2500	250	5.78
U_{inlet} $[\frac{m}{s}]$	20	2	0.46

Table 4.1: Molar fractions, mass flow rates of water and injection velocities for each case selected.

.

4.4. Fluid dynamic results

A few word and images can be spent on velocity fields and turbulent structures, in order to better understand the next results. From table 4.1 it's clear how the mass of water injected is important for the least concentrated case, in order to obtain the same discharge rate of calcium hydroxide of the other two conditions. Also the injection speed becomes important, thus probably affecting the flow in a significant way. From this point, a brief analysis of the fluid-dynamic of non reactive simulations has been conducted, by mainly relying on Q criterion for the visualization of vortices. This method represents a useful tool for analyzing fluid flow and is based on the concept of the strain rate tensor. This tensor describes how the fluid is deformed as it flows, and the Q criterion is derived from its second invariant. The Q criterion provides a scalar value that gives information about the local flow behavior, particularly with regard to vortices and their associated regions of intense fluid deformation. High Q values correspond to regions of intense vorticity and strong fluid deformation, while low Q values correspond to regions of low vorticity and fluid deformation. Negative values represents viscous stresses dominated areas. The Q criterion is often used in computational fluid dynamics simulations to identify and track vortices in the flow, which can be important for understanding various fluid phenomena and designing fluid systems. In order to provide an expression of Q, without going too deep into the explanation, we can define it as:

$$Q = \frac{1}{2}(||\Omega^2|| - ||S^2||) \tag{4.5}$$

where Ω, known as rotation tensor, is the antisymmetric part of the velocity gradient tensor, while S is the symmetric one, called strain rate tensor.
The next visualizations are referred to the last time step simulated, i.e. 8 seconds, in order to provide a certainly well developed flow. Starting from lateral slices (Figure 4.9), vortices are clearly visible in the wake region for all the three cases. It can be noted how the 2 g/l case is the only one that shows a different behaviour moving away from the propeller, while the other two conditions presents almost identical patterns.

Other information retrievable are given by slices orthogonal to x axis (Figure 4.10, taken respectively at 2, 4 and 5 diameters from the propeller. In all of three cases a predictable decaying of turbulent structures is appreciable. In these Figures, the different pattern of the first case, as the distance from the propeller increases, is more visible.

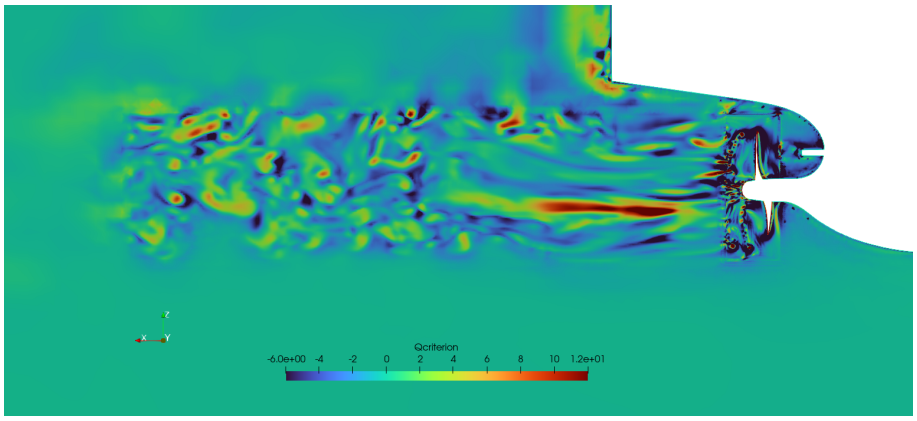

(a)

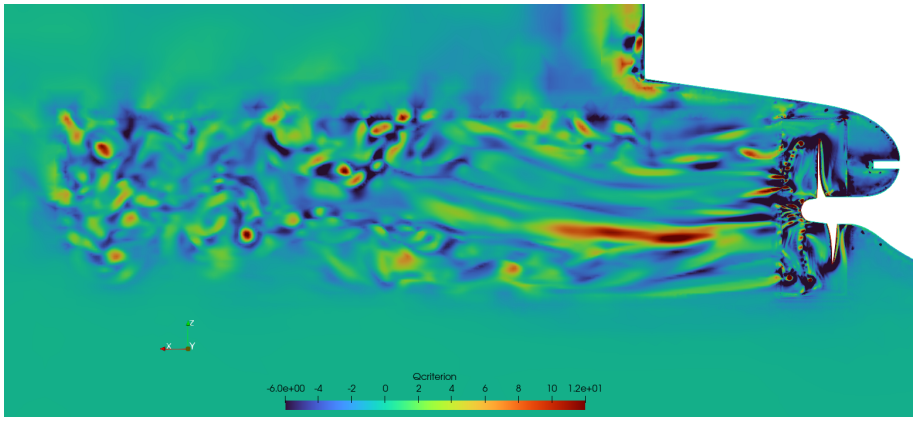

(b)

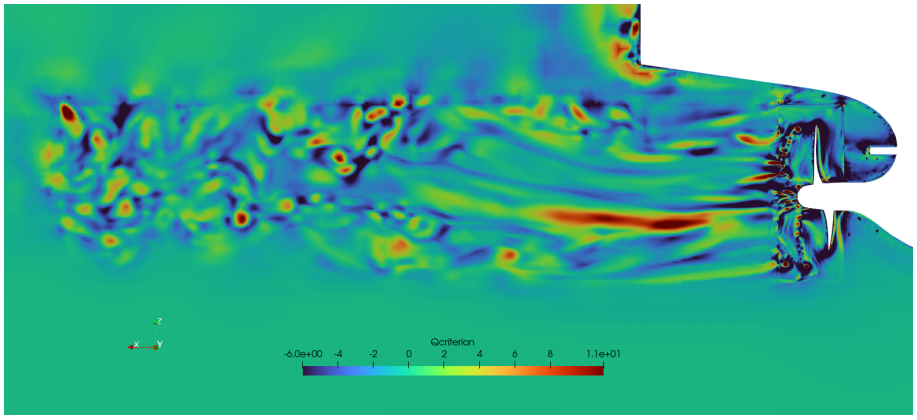

(c)

Figure 4.9: Side slices for each case representing Q values. (a) represents 2 g/l, (b) 20 g/l, (c) $86,5$ g/l.

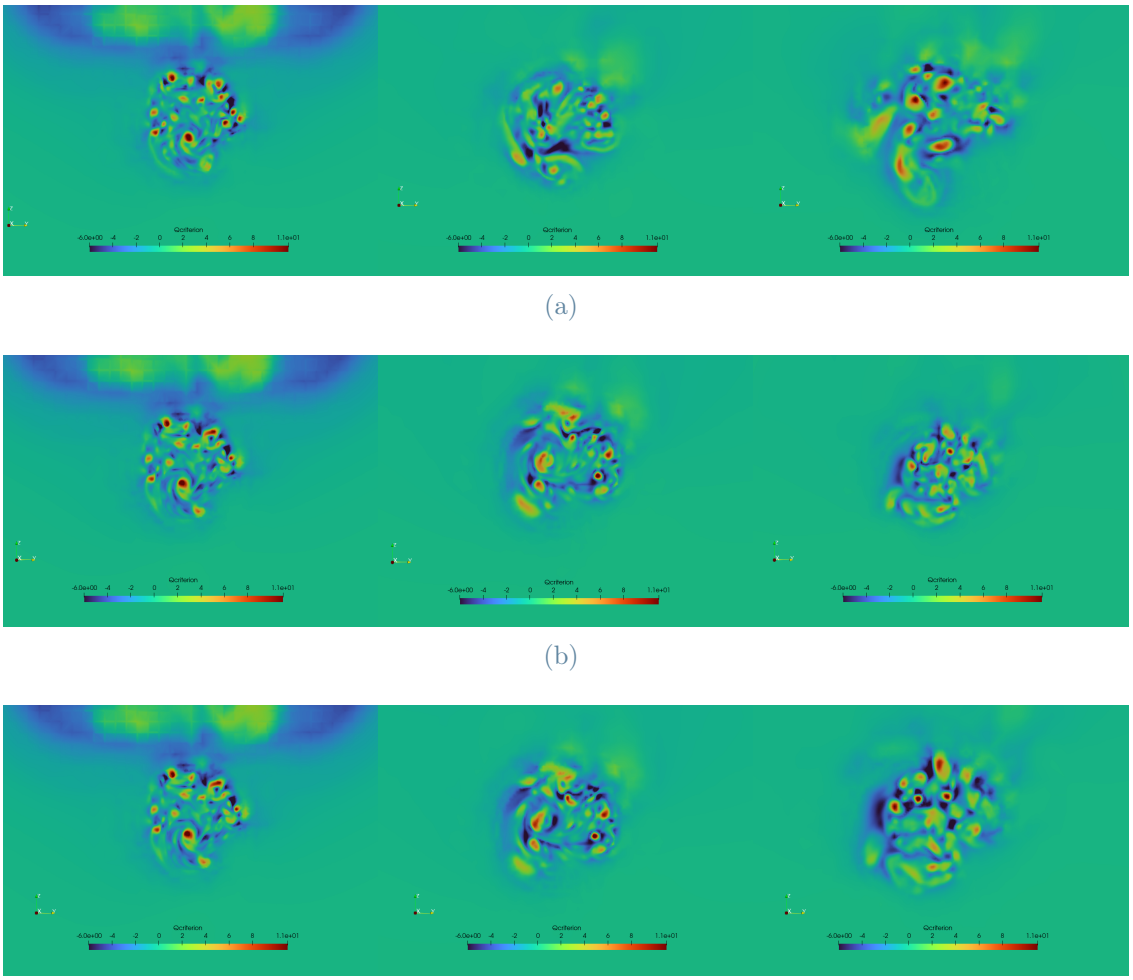

(a)

(b)

(c)

Figure 4.10: Front slices for each case representing Q values. (a) represents 2 g/l, (b) 20 g/l, (c) 86,5 g/l. From left to right, sections are taken at 2, 4 and 5 diameters from the propeller, respectively.

Even though some of the flow unsteadiness and hints of the vortical structures can be observed in each plane, planar cuts like those shown above are very limiting when attempting to portray the desired coherent structures which are inherently three-dimensional. To complete the picture then, iso-surfaces of Q has been extracted (Figure 4.11). It is also worth noting that as the value of Q increases, the number and detail of captured structures decreases. The resolution of the mesh also plays a key role in this technique: a very refined mesh allows much more detail to be observed, which is why the highly refined MRF area is too detailed to deduce any meaningful considerations. For the same value, however, the region immediately following the helix allows one to appreciate quasi-streamwise vortices, of variable diameter and size depending on the local velocity field and turbulent intensity, as well as the rotor wake and the swirl caused by the rotation as

the wake convects downstream. The water injected appears to influence the flow field in the first case, expecially in the distant wake, while it poorly contributes for the 20 and 80 g/l cases, creating coherent structures almost identical.

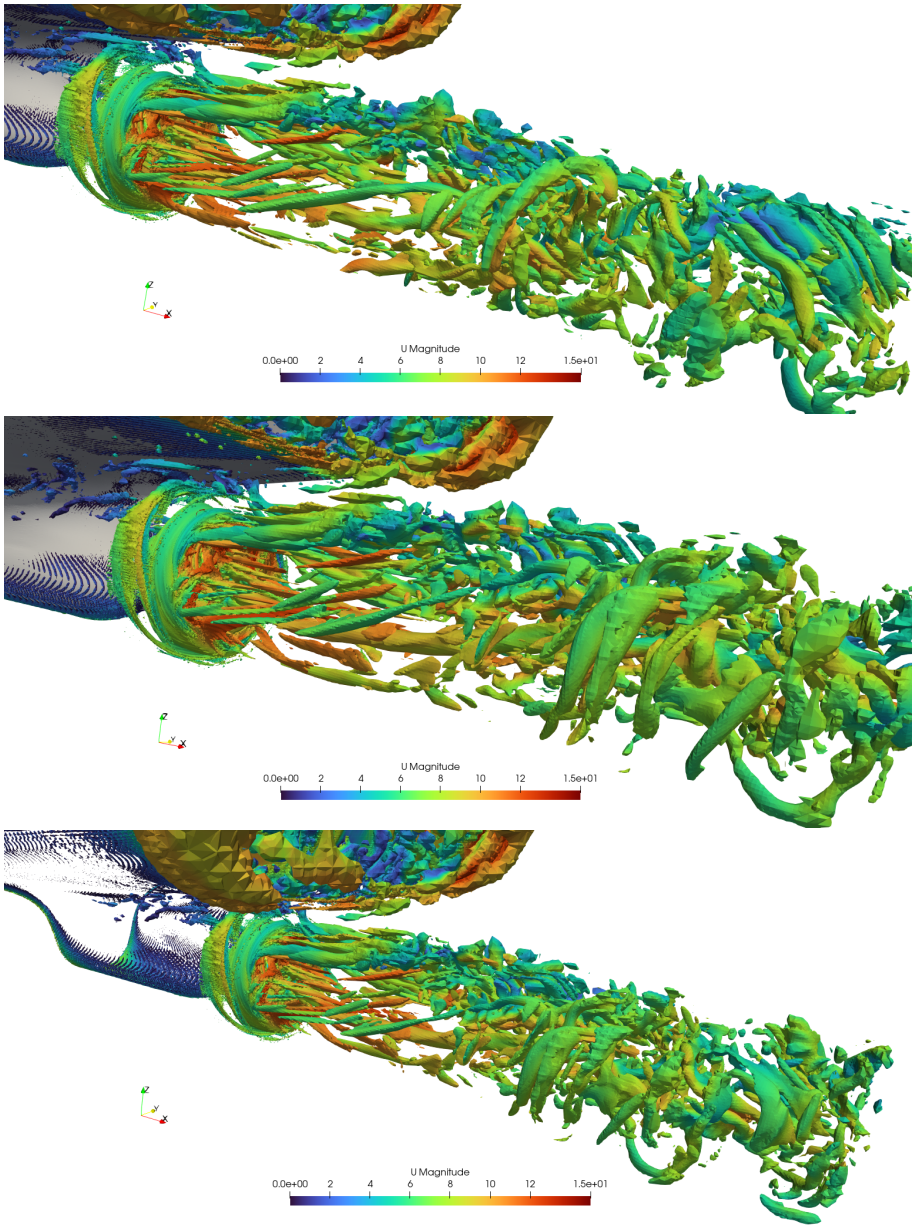

Figure 4.11: Iso-surfaces of $Q = 4$ for each case, respectively 2, 20 and 86 g/l.

4.5. Slaked lime discharge

At this point, visualizations of the non-reactive slaked lime diffusion are shown (Figure 4.12, in order to clearly see the phenomena for each case.

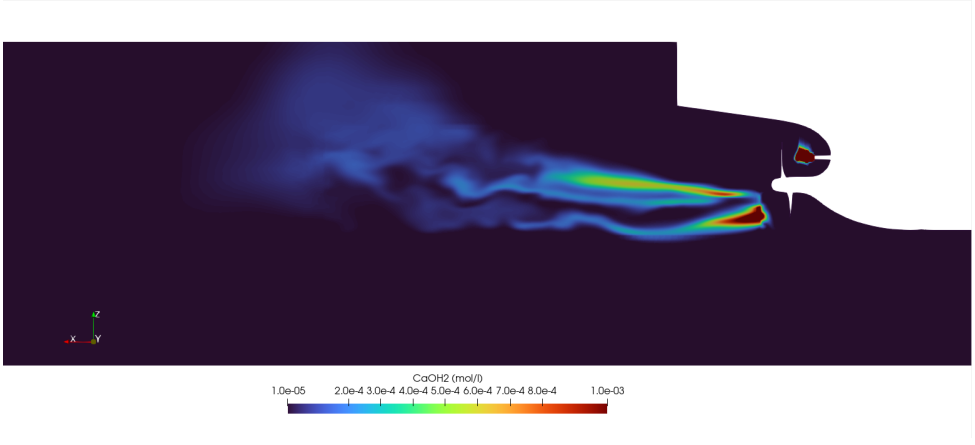

(a)

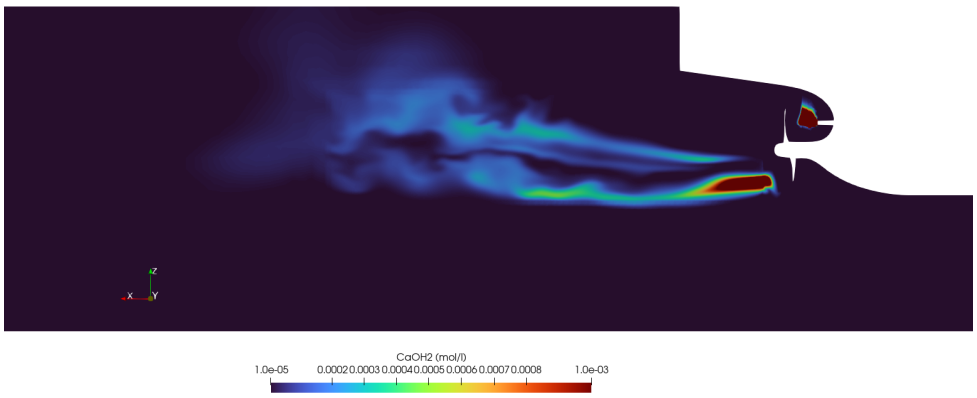

(b)

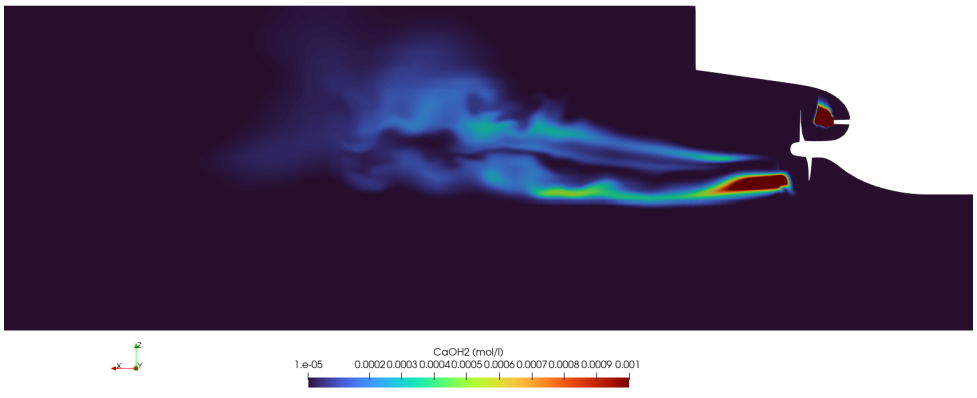

(c)

Figure 4.12: Side slices with $CaOH_2$ concentrations. (a) represents 2 g/l, (b) 20 g/l, (c) $86,5$ g/l.

Note how in the three figures the range of values presented is the same for each case,

providing meaningful comparisons. The injection velocity shows a great contribution for the lime's diffusion: in the first case, even if the initial concentration of lime injected is significantly lower with respect to the third case, a similar concentration pattern is visible, with the lime conveyed both by the injection and propeller's mixing effect. The second and third case don't show appreciable differences in the diffusion patterns, where the mixing is given only by the rotating motion induced by the KP505, which contributes to the sudden acceleration of the flow.
Other considerations can be made by looking at slices orthogonal to x axis (Figure 4.13, positioned respectively at two, four and five diameters from the propeller. As it can be seen from the Figure above, the three cases present an overall increase in the lime concentration if the initial concentration is increased too, as expected. Another observation is the progressive dispersion of $CaOH_2$ while moving away from the propeller, with the 2 g/l case showing lower values with respect to the other two conditions. Even from this perspective, only the first case presents different patterns of diffusion that becomes more pronounced moving away from the propeller.

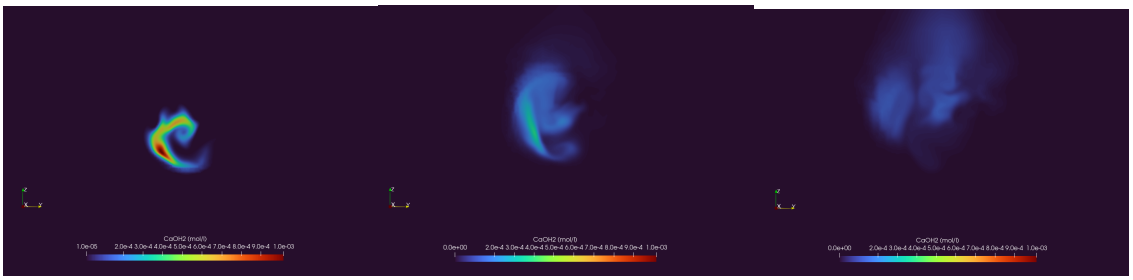

(a)

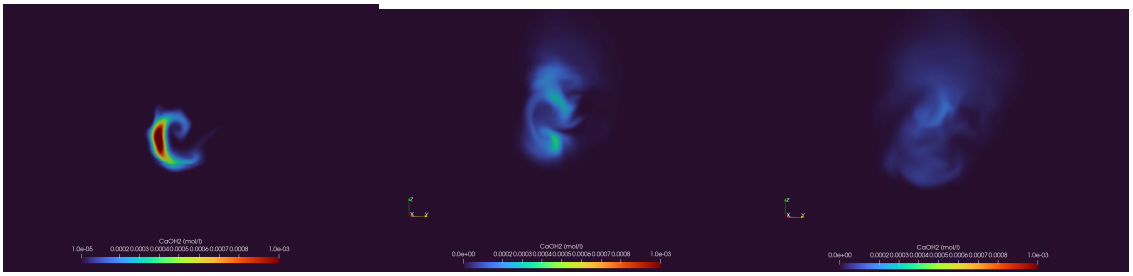

(b)

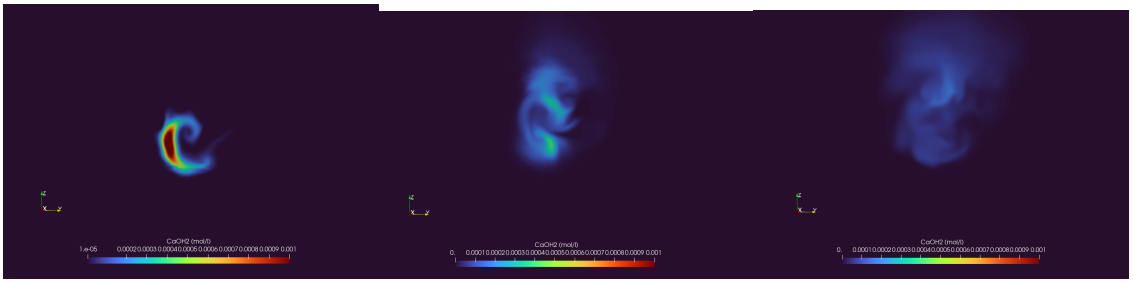

(c)

Figure 4.13: Front slices with $CaOH_2$ concentrations. (a) represents 2 g/l, (b) 20 g/l, (c) 86, 5 g/l. From left to right, sections are taken at 2, 4 and 5 diameters from the propeller, respectively.

Other meaningful data can be made when comparing the results with the reacting case, which will be presented in the following chapter.

5 | Reactive simulations

At this point, it's possible to furtherly analyze the simulations where chemistry is active. As already explained in chapter 4.3, three cases have been simulated: 2 g/l, 20 g/l, 86.5 g/l. Before presenting the results, however, a validation of the chemical model is presented.

5.1. Chemistry model validation

In order to lend greater credibility and stability to the data and observations that will be made later in this chapter, it was deemed of paramount importance to validate the model with pre-existing data. To this end, the data obtained from Abbate and Bianchi's work [2] on the 2 g/l case were used. The simulation was carried out by creating a simple two-dimensional reactor in which calcium hydroxide reacts with water.
The concentration of OH^- ions over time was then extrapolated by comparing the case with the data obtained by Abbate. As can be seen from Figure 5.1, the phenomena presents the same plateau value in both cases, as does the duration of the transient, although the precise chemical dynamic is not captured with perfect accuracy.
The model adopted is evaluated as adequate in order to simulate conditions where the solution is not oversaturated, as already pointed out in chapter 4.3. In fact, the presence of particles may deeply affect the characteristics of the transient phenomena.

5.2. Chemistry results

In this chapter the data obtained from the simulations will be presented. A focus on pH values will be discussed, as well as maximum and mean concentrations of OH^- ions and $CaOH_2$ diffusion. Comparisons between non-reacting and reacting cases will be shown. The physical time simulated for every case is 8 seconds, and the maximum Courant number has been set to 0.9 for the fluid-dynamic time steps and 0.3 for the local time stepping (section 2.3.2). All the data displayed, with except for the visualizations like contours and slices, are averaged over time using a code developed with Matlab, using

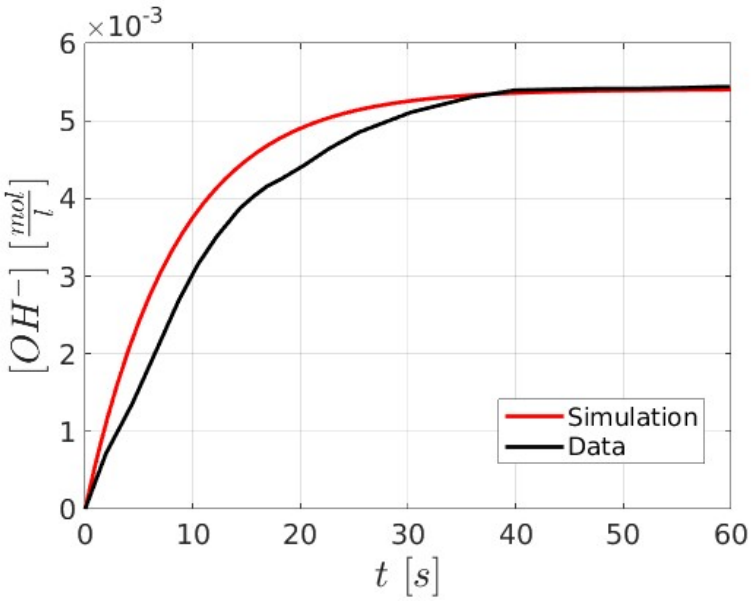

Figure 5.1: Molar concentration of OH^- ions over time, for simulated case and Abbate and Bianchi's data [2].

the same post-processing method adopted in chapter 4.2 for the mesh convergence. The pH value of seawater is 8.2, and the temperature has been set to 293 K.
First, a deep analysis of the carbon hydroxide distribution is given, making comparisons with the non reactive case and performing some statistical evaluation. Subsequently, the results concerning the concentrations of OH^- ions, both in average and maximum terms, will be presented, together with the pH values, the end point of the present work.

5.2.1. Slaked lime diffusion

In the present section, we supplement and improve the information provided in chapter 5.2.1, by analysing and comparing calcium hydroxide concentrations between reactive and non-reactive cases. It's important to stress that the next results are maximum values averaged over time.
In Figure 5.2, it is not possible to draw any particular meaningful observations, as the decrease in concentration due to the chemical phenomenon appears to be an order of magnitude too small compared to the concentrations introduced into the domain. One can only begin to appreciate differences due to chemistry in the case of the lowest concentration of slaked lime, i.e. that at 2 g/l. In all three cases, however, an expected trend can be observed: a hydroxide peak is formed at the inlet, followed by a decrease as one moves away from the propeller.

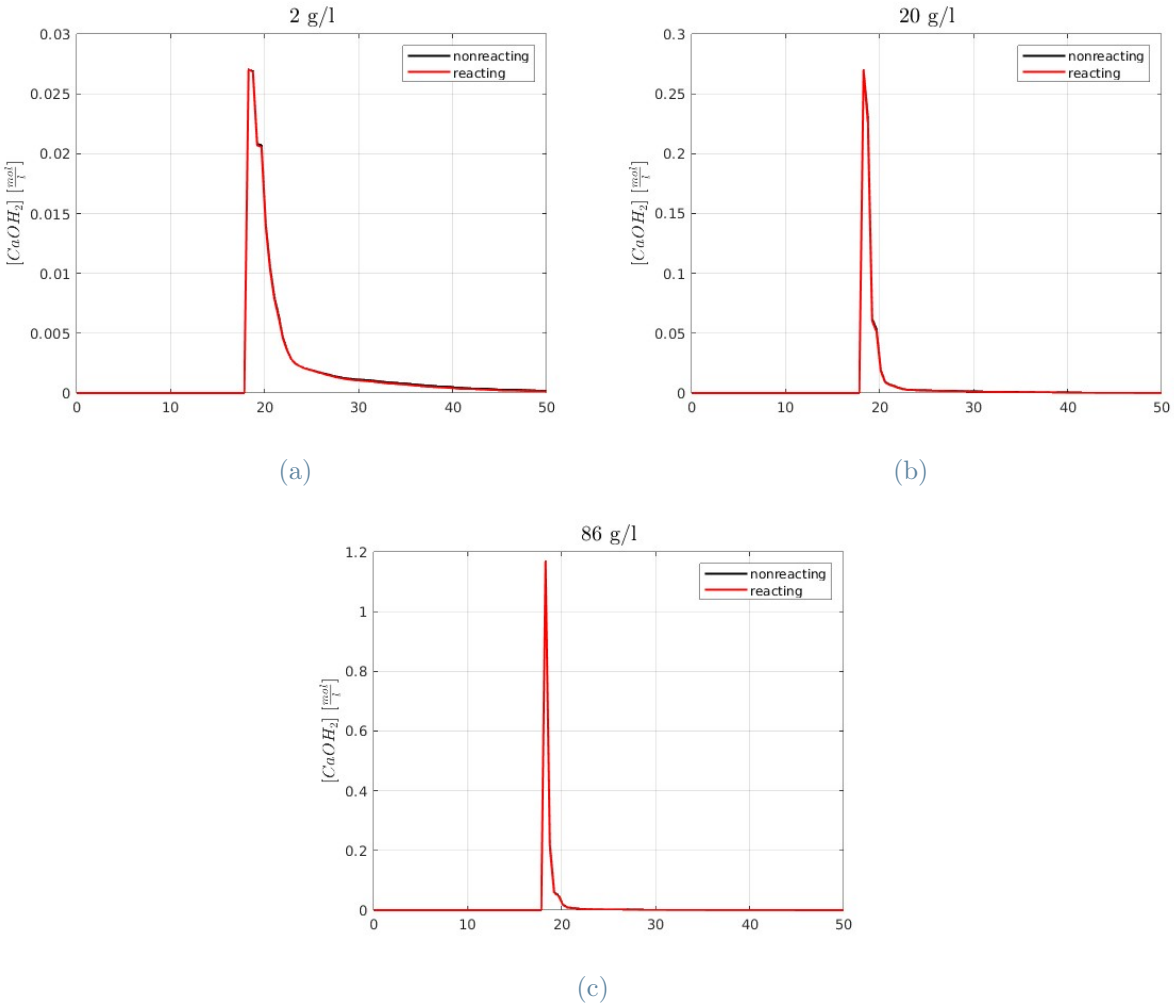

Figure 5.2: $CaOH_2$ maximum concentrations along x axis, averaged over time, for each case. Both non reacting and reacting cases are shown in the same plots.

In order to refine the analysis, in Figure 5.3 the variations due to chemical reactions are plotted, showing more informations regarding the phenomena. Variations are expressed as the difference between non reactive and reactive concentrations. As expected, a peak at the injector can be appreciated, showing however a different trend between the three cases. When the initial concentration is 2 g/l in fact, the maximum value curve has a first positive peak followed by a much smaller, but negative, second peak. After this region, the second part of the domain presents again a positive delta. This is due to the high speed at which the calcium hydroxide is injected into the water, advancing rapidly before being 'slowed down' by the stirring effect of the propeller. In the same case, moreover, the lime injected leads to a non-zero hydroxide delta until about 70m, showing a much larger portion of the domain where the chemical reactions are still present, in contrast

with the other two conditions.

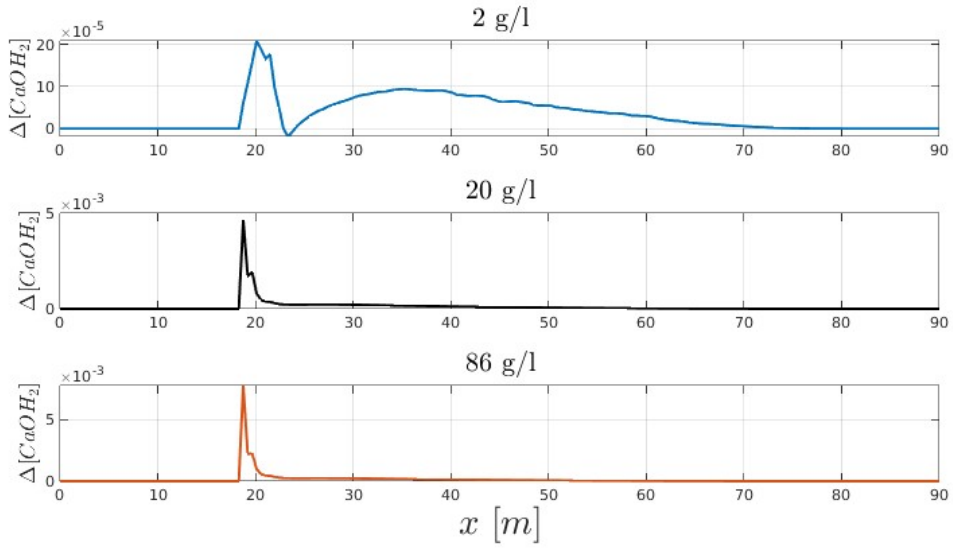

(a)

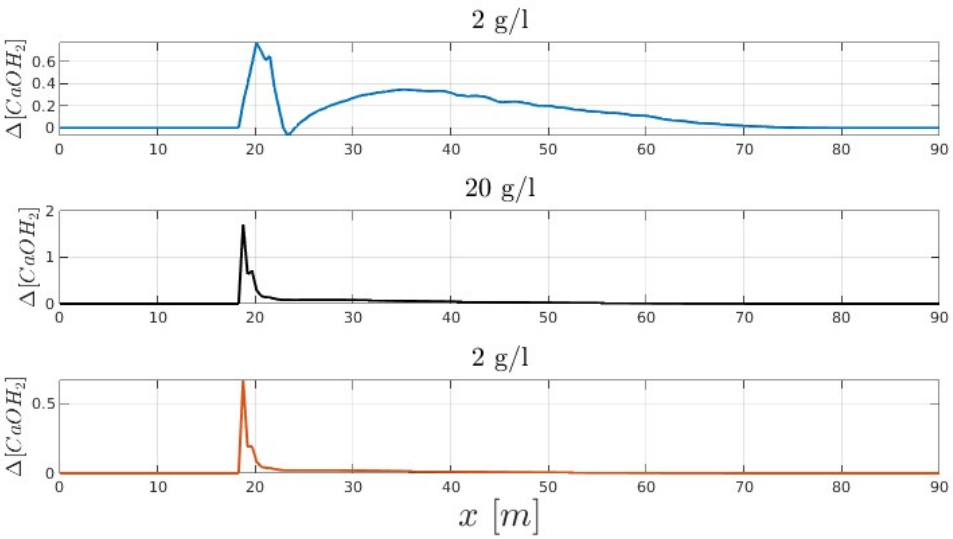

(b)

Figure 5.3: Plots of concentration's difference of slaked lime between non reactive and reactive cases, for each initial concentrations. In (b) the variations are reported in percentage with respect to the inlet values.

The time average must be justified in some way, so that a good degree of confidence can be placed in the proposed data. For this purpose, the root mean square of all data sets was calculated (Figure 5.4).

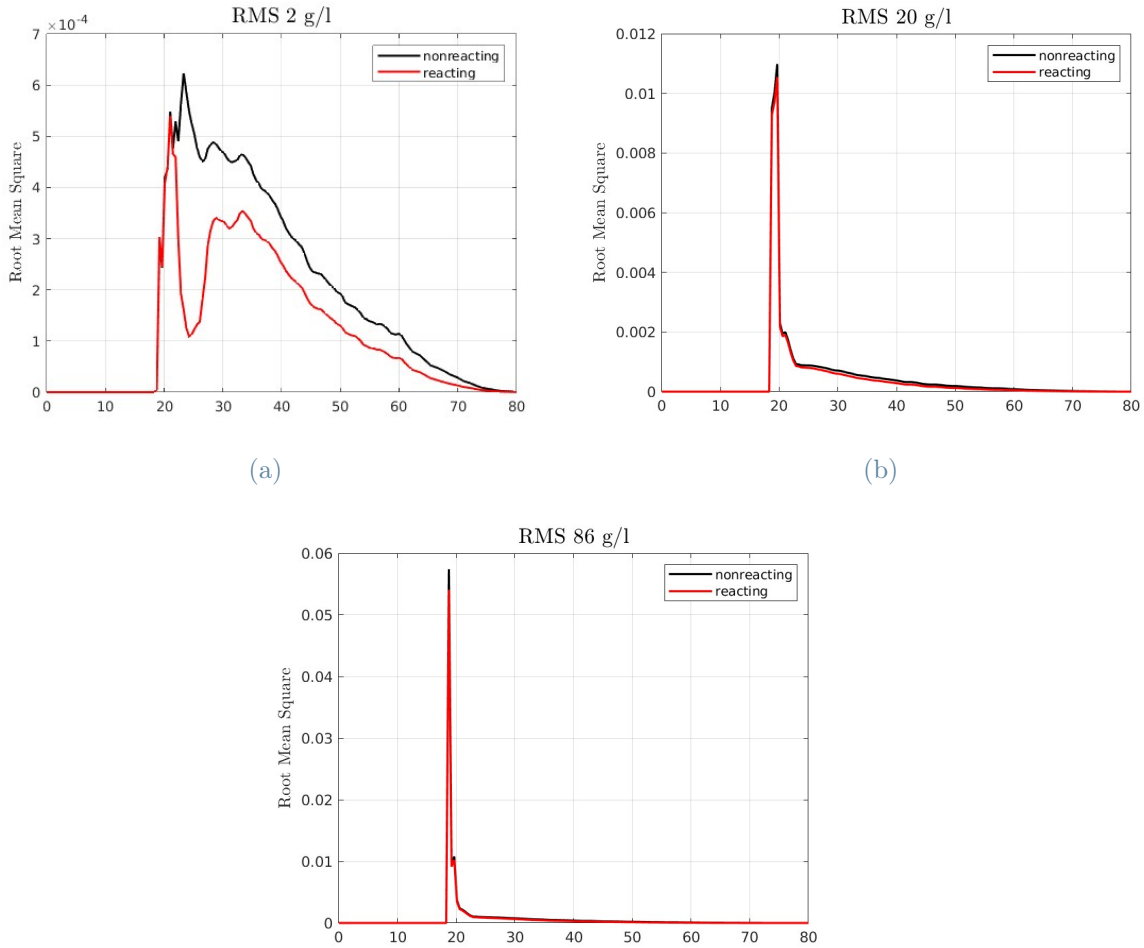

Figure 5.4: Root mean square of $CaOH_2$ maximum concentrations along x axis, averaged over time, for each case.

These plots show a fixed trend: the root mean square remains around 2% with respect to the maximum concentrations, thus providing a good degree of confidence to the time average performed. In the end, it can be noted how, for the 2 g/l case, the difference between the reactive and non reactive root mean squares are of greater magnitude, stressing again the effect of the injection on the flow field. From these figures it can be noted a crucial aspect that will be furtherly inspected in the next paragraph: with an high injection velocity, the region characterised by higher unsteadiness moves further, as visible also from Figure 5.5, representing the difference between the root mean squares calculated for reactive and non reactive cases.

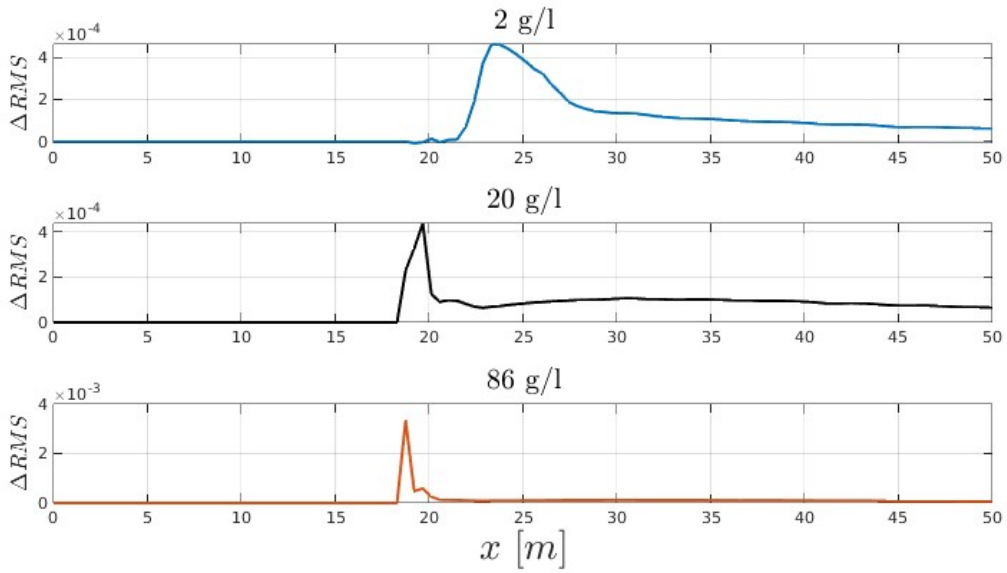

Figure 5.5: Difference between root mean squares for reactive and non reactive cases, for each injection condition.

5.2.2. pH distribution

The first results that will be displayed are the maximum values of OH^-, therefore pH. Next, mean values will be taken into account for more observations. As visible from Figure 5.6, the conclusions that can be drown are similar to the ones made for the calcium hydroxide diffusion: after a peak at the propeller, the concentration of ions diminishes to zero. For the first two cases in Figure, the decrease is very steep in space, while the 2 g/l case, due to the high speed of injection, takes about 70 m to reach an almost null value. It should also be noted that the peak in the last case is shifted a few metres further, for the same reason presented above. This trend can also be observed in the graph of the maximum pH, in Figure 5.7.

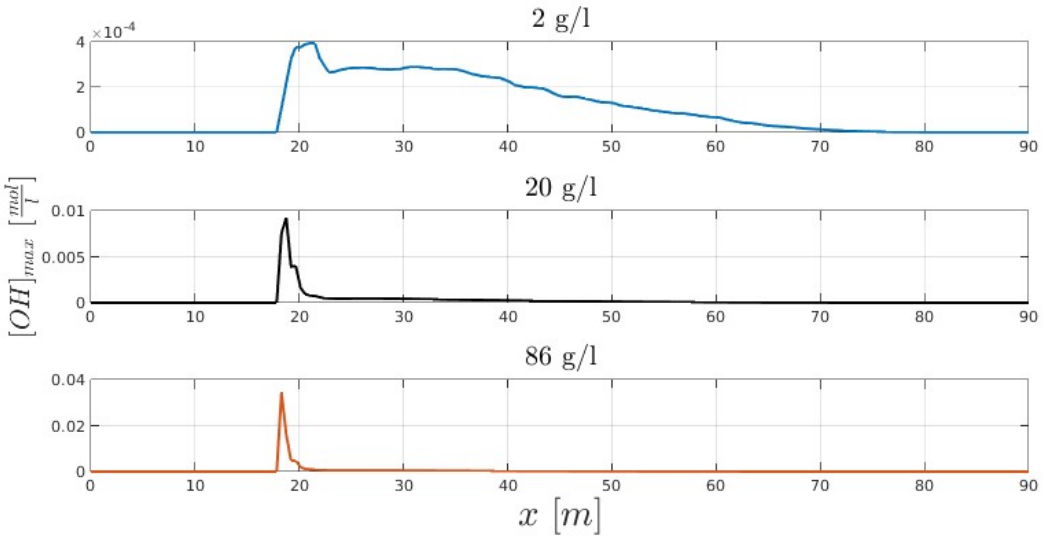

Figure 5.6: Maximum OH^- concentrations for the three cases simulated along x axis.

In Figure 5.7, the three peaks show a predictable trend: by increasing the concentration of $CaOH_2$, the pH reached is higher, reaching a maximum value overall of 12.5. From this graph, a new trait of the phenomenon emerges: after a first peak, different from every case, the behavior becomes similar across the different conditions, leading to almost identical values that reach standard pH by the end of the domain. In detail, we can appreciate the same shift encountered in Figure 5.6 for the case at 2 g/l: the maximum is reached a few metres later, with a less marked decrease along the direction of movement.

As done in chapter 5.2.1, in Figure 5.8 the root mean square for the maximum concentrations has been computed, showing, in contrast with the previous analysis, values around $10 - 25\%$ which highlight a strong unsteadiness of the phenomena.

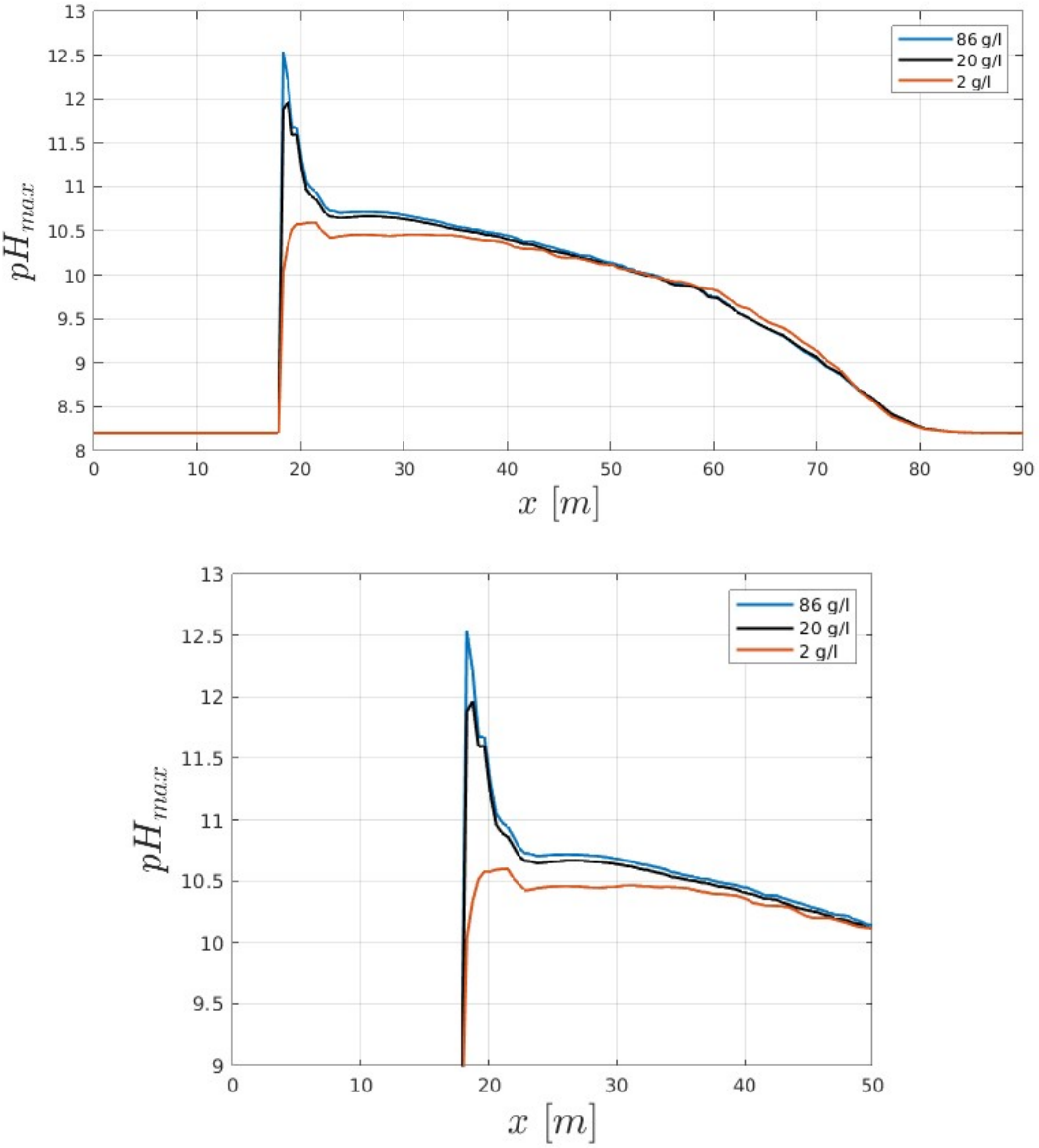

Figure 5.7: Maximum pH along x axis: in the second picture a detail of the peaks is presented, in order to appreciate both the values reached and the spatial distribution.

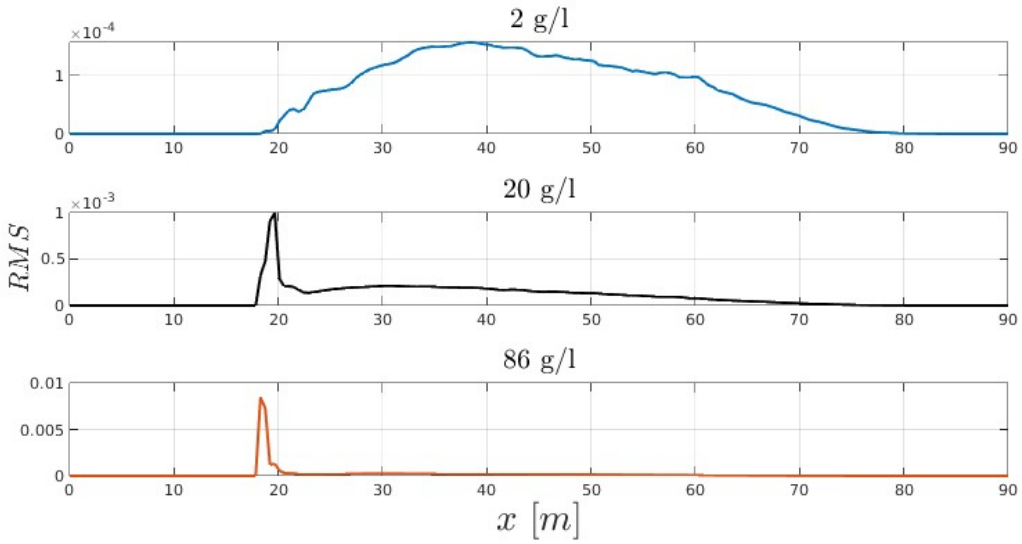

Figure 5.8: Root mean square of maximum OH^- concentrations for the three cases simulated along x axis.

Continuing the analysis, it is also appropriate to observe the mean OH^- and pH distribution, visible in Figures 5.9 and 5.10. From this point of view the first peak is completely absent for the least concentrated simulation, while the most concentrated one departs greatly for the first peak. The mixing effect in the first part of the wake is responsible for the similar and close trend of the three plots, particularly after 30 m, where pH values are almost identical for the latter part of the domain. As observed in Figure 5.7, the case at 86 g/l maintains a higher value of pH up to the end of the region simulated.

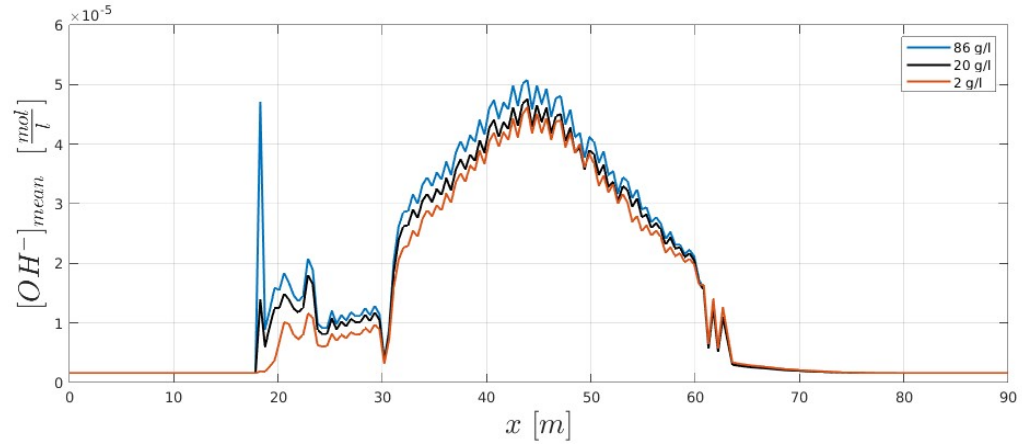

Figure 5.9: Mean OH^- concentrations for the three cases simulated along x axis.

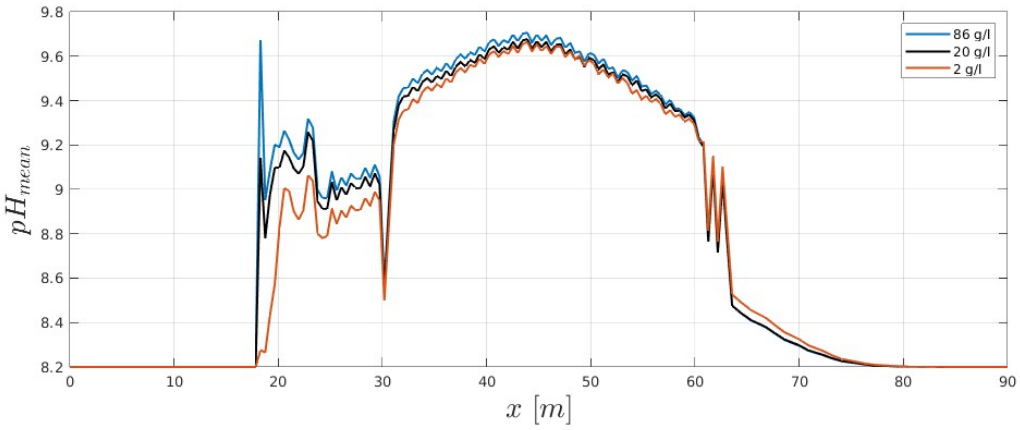

Figure 5.10: Mean pH values for the three cases simulated along x axis.

The unsteadiness of the problem also shows its weight in this analysis, with higher values of RMS than in the analysis of the maxima, especially in the second part of the domain, clearly a zone with higher convection and diffusion.

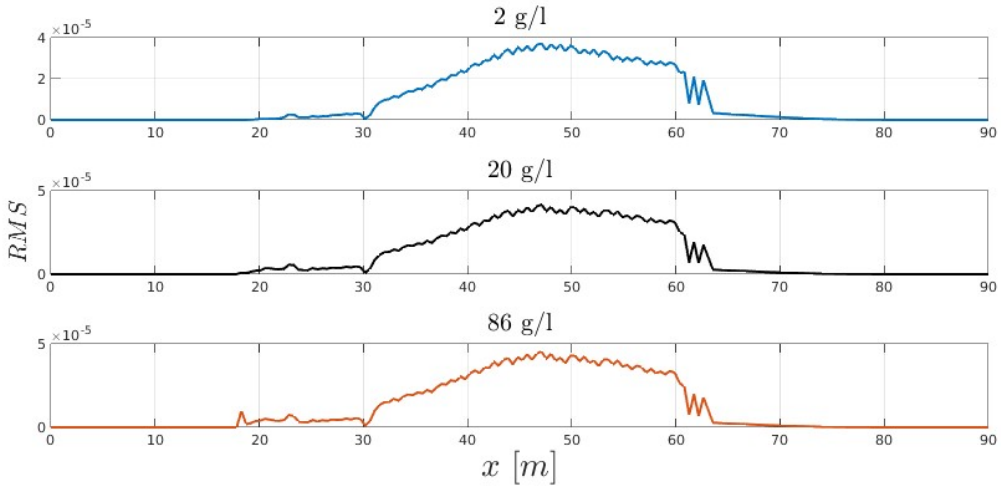

Figure 5.11: Root mean square of mean concentrations for the three cases.

At this point of the analysis, a tridimensional visualization of the problem can help understand more clearly the phenomena. All the Figures refer to the last step of the simulations, i.e after 8 s, which can represent the most developed flow obtained. From 5.12, the effect of injection velocity is clearly visible for the 2 g/l case, contributing to high values of pH even quite far from the propeller. Furthermore, the second and third slice shows almost identical patterns with just a small increase in the pH values.

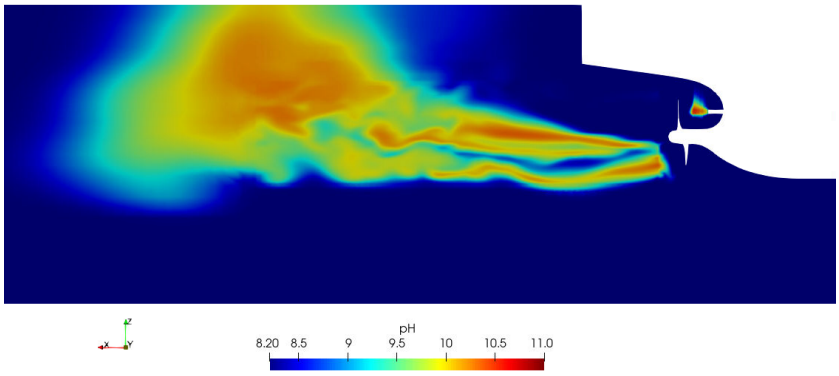

(a)

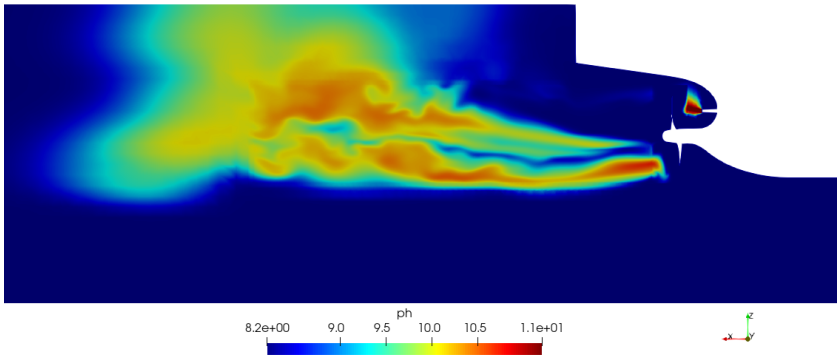

(b)

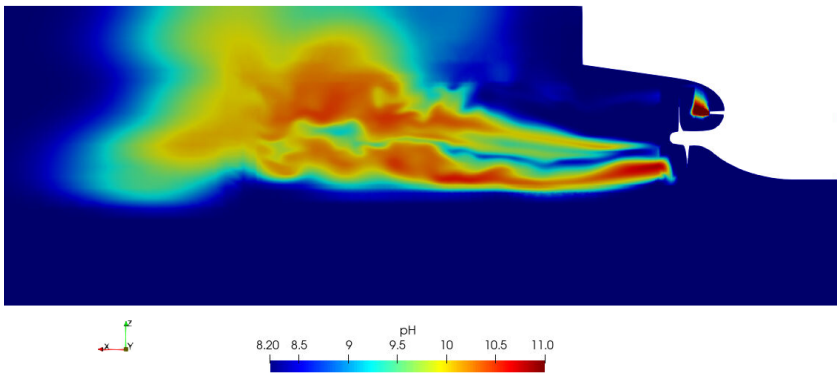

(c)

Figure 5.12: Lateral slices of the domain showing pH values 8 seconds after the injection of slurry, respectively for 2 (a), 20 (b) and 86.5 g/l (c).

The most critical zone for the reported analysis is the one located approximately between 40 and 60 metres from the beginning of the simulated region, characterised by great

diffusion. Its size and extent can be appreciated in the following contours, initially shown for each case taken individually (Figure 5.13). There are three contours for each case, with the same constant pH values for each curve: 9, 10 and 10.5. The blue curve represents a pH value of 9, while the orange and red respectively 10 and 10.5.

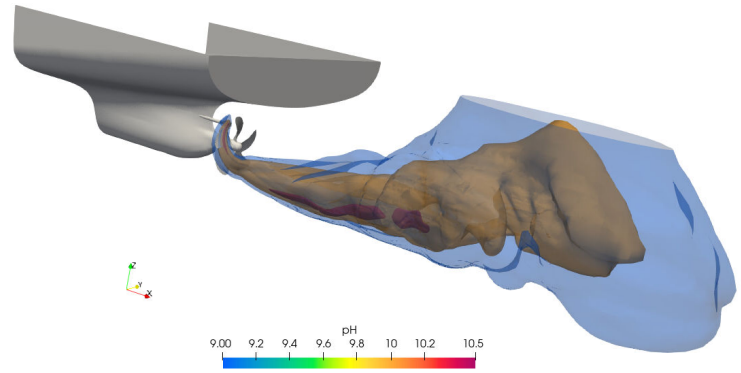

(a)

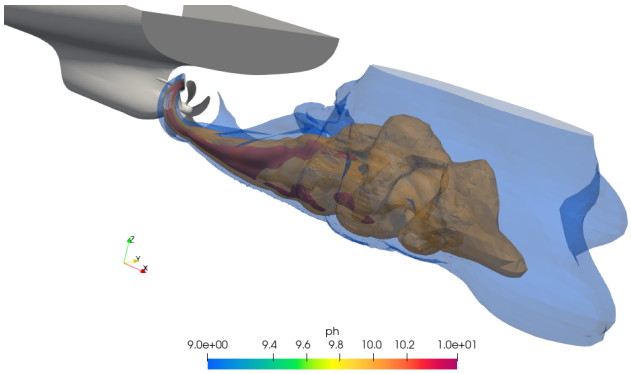

(b)

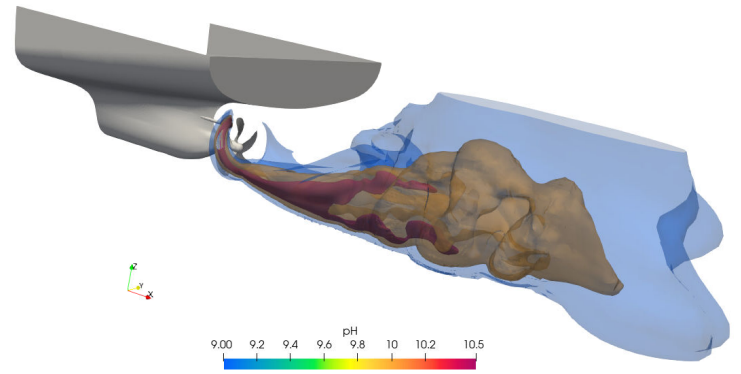

(c)

Figure 5.13: Contours of pH values for 2 (a), 20 (b) and 86.5 g/l (c) cases.

In each of the three cases, higher pH concentrations represent relatively smaller portions

of the wake, as was to be expected, especially for the case at 2 g/l. As already anticipated by previous plots, the two cases with greater initial concentration have very similar behaviours, and both show a large portion of the sea with a pH of 10, characterised by structures that follow the rotating wake motion, while the 2 g/l case, since the concentration is lower, appears to be less influenced by the stirring effect of the propeller only because the iso-surface remains inside the shear layer. For each of the three cases, extremely high pH remains confined to small, near-propeller regions. If Figure 5.13 allows us to see different pH values compared between the cases, the observations made so far can be visualised even more clearly by looking at the Figures 5.14, 5.15 and 5.16, where contours at the same pH are compared for each case. The colour code used should be noted:

- **red curves**: represent 2 g/l case;
- **yellow curves**: represent 20 g/l case;
- **blue curves**: represent 86.5 g/l case.

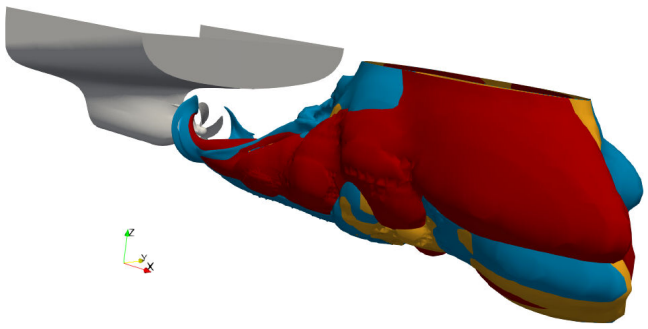

Figure 5.14: Comparisons between contours at 9 pH value for different cases.

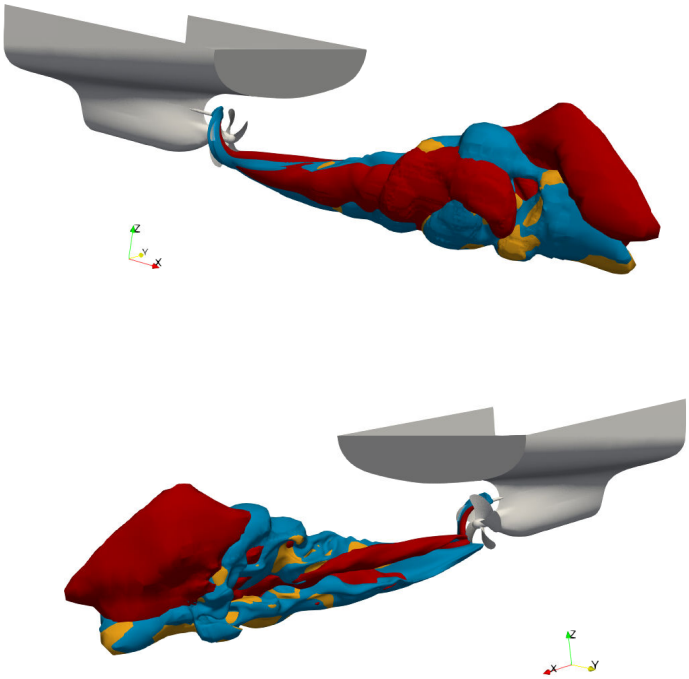

Figure 5.15: Comparisons between contours at 10 pH value for different cases.

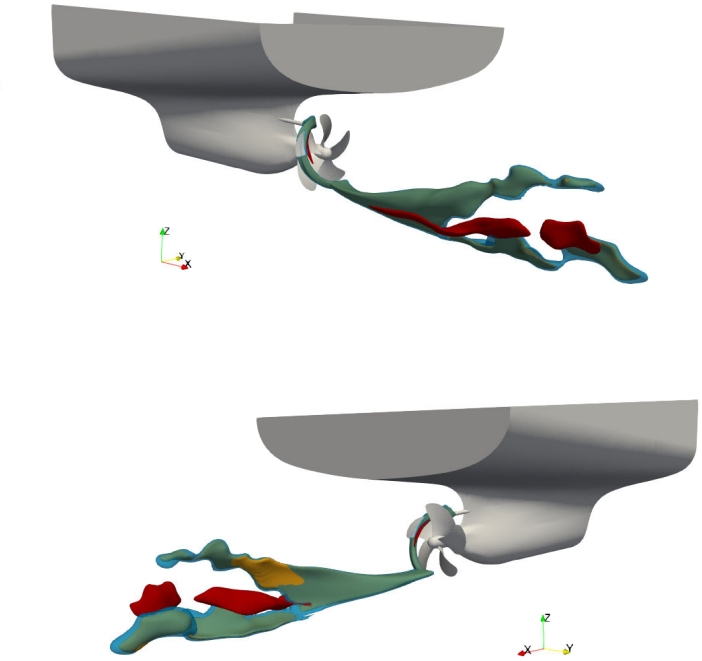

Figure 5.16: Comparisons between contours at 10.5 pH value for different cases.

From Figure 5.14, it can be seen how the plume at pH=9 extends similarly for all the three cases simulated, as already confirmed by plots in Figures 5.7 and 5.10. The maximum distance reached from the propeller is about 60 m, with a maximum width of 14 m. In Figure 5.15, this region with high pH extends for 53 m in length and 8 m of width. In this visualization it can be appreciated how the 20 and 86.5 g/l cases present iso-surfaces more influenced by the rotating motion of the propeller. In the end, in Figure 5.16, the regions with high pH are significantly less extensive, with thin iso-surfaces 30 m long for each case. The potential harm for marine biota, given these extended region at high pH, should be investigated.

6 | Conclusions and future developments

This final chapter will provide further observations and evaluations about the project. Starting from considerations regarding each case:

- **2 g/l**: this condition requires a lot of water to be injected, hardly feasible with current ships, thus requiring a readaptation of systems and implants adopted until now. The injection jet influences the field of motion, delaying the peak of reaction for example, while the low initial concentration avoids very high peak of pH in the very first region of the wake;
- **20 g/l**: the mass flow rate of water is smaller by an order of magnitude than the previous case, hence it could be more practical at an actual design stage. This case also presents analogous trend to the 2 g/l case, with only a first peak of maximum that constitutes an actual difference;
- **86 g/l**: this operative condition keeps high values of mean and maximum pH in the first region of the domain, and shares almost identical patterns with the second case presented. The diffusion is completely driven by the stirring effect of the propeller. It is not clear if a pH value of 12.5, even if confined in a very small region, could represent a source of harm for marine biota.

All the cases return back to standard values within 80 meters.
The tests performed are promising, providing reliable results on the chemical characteristics as well as the fluid dynamics of the problem. However, the analysis could be improved in many respects, depending on the objective. Sticking with analysing the near-wake zone with an LES approach for the modelling of turbulence, with the improvement of computational resources, the entire domain, or a significantly larger portion, should be simulated with a higher degree of refinement. In this way, it would be possible to capture turbulence structures with greater precision, but above all to reduce the inhomogeneity of the grid, which can lead to calculation and discretisation errors.
The unsteadiness of the phenomenon is certainly a problem that needs to be addressed,

as can be seen from the RMSs for the $[OH^-]$ concentrations. By simulating for a longer time, thus obtaining more data, it would be possible to increase the degree of confidence in the results obtained. Speaking of the case with the highest concentration, which must be remembered to be in a saturation condition, in order to provide an adequate term of comparison to results obtained previously (Caserini et al. [4]), it would be appropriate to simulate the solution with a dispersion of molecules within it, as in the physical reality of the problem. In this way, however, it would be necessary to consider more in-depth and detailed chemical kinetics, as well as a more complex particle-flow interaction. These kinds of simulations, known as Lagrangian simulations, can become extremely expensive in terms of computing resources, and certain compromises would have to be made in order to perform a feasible simulation.

Bibliography

[1] Kcs ship data: hull geometry. http://www.simman2008.dk/KCS/kcs_geometry.htm, accessed 2023-4-14.

[2] S. Abbate and R. Bianchi. Large eddy simulation of the flow in a stirred tank reactor for calcium hydroxide dissolution. Master's thesis, Politecnico di Milano, 2021.

[3] N. L. Bindoff, W. W. L. Cheung, J. G. Kairo, et al. Changing ocean, marine ecosystems, and dependent communities. *IPCC Special Report on the Ocean and Cryosphere in a Changing Climate*, pages 545–546, 2019.

[4] S. Caserini, D. Pagano, F. Campo, A. Abbà, S. de Marco, D. Righi, P. Renforth, and M. Grosso. Potential of maritime transport for ocean liming and atmospheric CO2 removal. *Frontiers in Climate*, 2021. doi: 10.3389/fclim.2021.575900.

[5] A. J. Chorin. A numerical method for solving incompressible viscous flow problems. *Journal of Computational Physics*, 1997.

[6] H.-T. Chou. On the dilution of liquid waste in ships. *Journal of Marine Science and Technology*, pages 149–154, 1996.

[7] CINECA. Galileo100 hardware. https://www.hpc.cineca.it/hardware/galileo100, accessed 2023-2-18.

[8] S. C. Doney, V. J. Fabry, R. A. Feely, and J. A. Kleypas. Ocean acidification: The other co2 problem. *Annual Review of Marine Science*, 1(1):169–192, 2009. doi: 10.1146/annurev.marine.010908.163834. URL https://doi.org/10.1146/annurev.marine.010908.163834.

[9] F.Argentieri. A three-dimensional non-reactive fluid dynamics model of the dispersion of calcium hydroxide in the wake of a marine propeller. Master's thesis, Politecnico di Milano, 2020.

[10] M. Germano. A proposal for a redefinition of the turbulent stresses in the filtered navier–stokes equations. *The Physics of Fluids*, 1986.

[11] Global Ocean Data Analysis. A uniformly calibrated open ocean data product of inorganic and carbon-relevant variables. `https://www.glodap.info/`, accessed 2023-1-26.

[12] H. Kheshgi. Sequestring atmospheric carbon dioxide by increasing ocean alkalinity. *Energy - The International Journal*, pages 20:915–922, 1995. doi: https://doi.org/10.1016/0360-5442(95)00035-F.

[13] KRISO. Kcs ship data: Propeller openwater data. `https://simman2020.kr/download/KCS-Propeller-Openwater-data-KRISO.dat`, accessed 2023-2-2.

[14] M.Copercini and F.Cusmai. Ocean liming: a LES analysis of feasibility and effect of discharging slaked lime in the wake of a ship. Master's thesis, Politecnico di Milano, 2021.

[15] E. Naudascher. Flow in the wake of self-propelled bodies and related sources of turbulence. *Journal of Fluid Mechanics*, pages 2:625–656, 1965.

[16] OpenFOAM Foundation. Openfoam9 user guide. `https://openfoam.org/version/9/`, accessed 2023-2-18.

[17] OpenFOAMWiki. Navier-stokes formulation in the rotating frame. `https://openfoamwiki.net/index.php/See_the_MRF_development`, accessed 2023-3-3.

[18] R. Pachauri, L. Meyer, et al. Climate change 2014: Synthesis report. contribution of working groups i, ii and iii to the fifth assessment report of the intergovernmental panel on climate change. *IPCC*, pages 545–546, 2019.

[19] T. Poinsot and D. Veynante. Theoretical and numerical combustion. *Prog. Energy Combust. Sci.*, 28, 01 2005.

[20] L. Prandtl. 7. bericht über untersuchungen zur ausgebildeten turbulenz. *Zammzeitschrift Fur Angewandte Mathematik Und Mechanik*, 5:136–139, 1925.

[21] P.Sagaut. Large eddy simulation for incompressible flows. *Springer*, 2006.

[22] P. Renforth and G. Henderson. Assessing ocean alkalinity for carbon sequestration. *Reviews of Geophysics*, pages 636–674, 2017.

[23] J. Smagorinsky. General circulation experiments with the primitive equations. *Monthly Weather Review*, pages 91(3):99–165, 1963.

[24] S.Pope. Turbulent flows. *Cambridge University Press, Cornell University*, 2000.

[25] Union of Concerned Scientists. CO2 and Ocean Acidification: Cause, Impacts, Solutions. https://www.ucsusa.org/resources/co2-and-ocean-acidification, accessed 2023-1-20.

List of Figures

List of Tables

Acknowledgements

Per iniziare ringrazio la professoressa Antonella Abbà, per il supporto datomi lungo questi mesi di lavoro, la disponibilità e la tranquillità dimostrata anche in momenti di tensione. Allo stesso tempo ringrazio anche il professor Federico Piscaglia per l'aiuto e il confronto su argomenti che non avevo, e non ho probabilmente, ancora padroneggiato al meglio. Un grazie va anche a Riccardo Bianchi e Samuele Abbate, che mi hanno aiutato a gettare le basi della tesi e condiviso la loro esperienza. Ringrazio infine il centro di calcolo CINECA per l'utilizzo del super-computer Galileo, senza il quale un progetto di queste dimensioni non si sarebbe potuto portare a termine.

Il progetto di tesi rappresenta la conclusione di un percorso accademico lungo anni, durante il quale più persone hanno percorso un pezzo di strada accanto a me, per poi allontanarsi silenziosamente in alcuni casi. Altre sono ancora qui. Vorrei ringraziarle tutte, in particolar modo la mia famiglia. Mia madre, mio padre, mio fratello sono stati preziosi e indispensabili, ma il sentimento non si limita, ovviamente, soltanto a loro.

Ringrazio anche tutto ciò che mi ha dato tanto oltre le classi dell'ateneo: La Terna Sinistrorsa mi ha permesso di coltivare insieme qualcosa, che tutt'ora dà i suoi frutti, ogni anno. Grazie agli amici di una vita: a Francesco, Alberto, Paolo. Grazie a Luna.

Sono veramente grato di tutto questo.

Buona fatica a me e a tutti voi.